Dynamical transverse laser patterns. I. Theory

M. Brambilla,* M. Cattaneo, L. A. Lugiato, R. Pirovano, and F. Prati*
Dipartimento di Fisica dell'Universitá di Milano, via Celoria 16, 20133 Milano, Italy

A. J. Kent and G.-L. Oppo
Department of Physics and Applied Physcis, University of Strathclyde, 107 Rottenrow, Glasgow, G4 0NG, Scotland, United Kingdom

A. B. Coates and C. O. Weiss
Physikalisch-Technische Bundesanstalt, 3300 Braunschweig, Germany

C. Green, E. J. D'Angelo, and J. R. Tredicce†
Department of Physics, Drexel University, Philadelphia, Pennsylvania
(Received 30 September 1992; revised manuscript received 21 June 1993)

We consider a cylindrically symmetrical laser with spherical mirrors and describe the dynamics in terms of the competition among different Gauss-Laguerre modes of the cavity. In this paper we focus on the case in which the mode competition leads the laser to a dynamical state that, according to the values of the control parameters, can be periodic or quasiperiodic. The linear stability analysis of the single-mode stationary solutions, in which the laser oscillates with the fundamental TEM_{00} or the TEM_{01}^{*} mode, provides an initial guideline in our search for the various spatiotemporal patterns which emerge. We consider cases in which the gain line activates one, two, or three frequency-degenerate families of modes. The motion of optical vortices, from the simple rotation to creation and annihilation in pairs is analyzed, together with the correlated movement of the peaks of the intensity distribution in the traverse plane. We study also the patterns which appear when the cylindrical symmetry of the system is broken. The parameters of our calculations correspond closely to those which characterize Na_2 lasers, CO_2 lasers, and Nd-doped yttrium aluminum garnet lasers.

PACS number(s): 42.60.Mi, 42.65.−k, 42.50.Lc

I. INTRODUCTION

In this paper we provide a description of a research area which is by now emerging as a new branch of nonlinear optics. It is well known that lasers show a tendency to develop nontrivial transverse configurations of the radiated beam. This feature is usually viewed as undesirable, both because these effects do not initially seem easily controllable, and because, for the sake of many applications, simple Gaussian TEM_{00} structures are preferred. For these reasons apertures and other means are used to restrict the size of the beam. However, recent years have brought an increasing consciousness that spatial and spatiotemporal effects in the transverse structure of the radiation field represent interesting phenomena *per se,* especially when the Fresnel number of the laser becomes large and allows the formation of complex patterns. Then spatial structures, defects, and turbulence arise spontaneously. These phenomena bear a striking resemblance to those found in other research fields such as hydrodynamics, nonlinear chemical reactions, and biology. Optics offers the additional possibility of controlling the number of modes in play, so that a wide variety of behaviors, from single modes to phenomena involving an extremely large number of modes, can be observed. Their relevance in optics is magnified by the perspective of future applications, which arise from the possibility of encoding information in the transverse structure and processing it in a completely optical and parallel way.

Investigations of transverse phenomena have addressed both passive systems without population inversion [1–8] and active systems such as lasers [9–29]. In the theoretical description of nonlinear optical systems, transverse effects appear as soon as one abandons the usual plane-wave approximation and allows for the transverse variation of the electric field governed by diffraction which, in the paraxial approximation, is described by the transverse Laplacian. In these systems diffraction, the counterpart of diffusion in chemistry and biology, plays a dominant role. As a matter of fact, a formal analogy between the laser equations and those of hydrodynamics has recently been demonstrated [18,28].

In this paper we focus on the case of a cylindrically symmetrical laser with spherical mirrors, and describe the dynamics in terms of the competition among different Gauss-Laguerre modes of the cavity. It must be kept in

*Also at Physik Institut, Universität Zürich, Zürich, Switzerland.

†Present address: Institut Nonlineaire de Nice, 1361 Route des Luccioles, Valbonne 06560, France.

mind that the modal amplitudes are a set of complex order parameters, and their phases play a role no less important than their moduli. A recent paper [30a] shows that the Gauss-Laguerre modes represent an appropriate basis for many laser states.

A prominent feature of the laser patterns is the presence of pointlike defects called *optical vortices* because of their similarity to vortex structures which are commonplace, for example in hydrodynamics, superconductivity, or superfluidity. In the case of optical systems, this kind of defect was first described by Berry and collaborators in the framework of *linear* wave equations [31]; more recently, in analyzing the laser model of Ref. [10], Coullet, Gil, and Rocca showed that these structures can be formed *spontaneously* by the nonlinear dynamics of the laser [26]. This fact was later confirmed by some of us in a more realistic laser model [27,17,29,30b]. The term "optical vortex" or "phase singularity" arises from the behavior of the gradient of the field phase $\nabla\Phi$, which exhibits vortex structures centered at points of the transverse plane where $\nabla\Phi$ diverges; as a matter of fact, the quantity $\nabla\Phi$ plays the same role as the velocity field in hydrodynamics in the case of the laser [18]. Because the Poynting vector of the radiation field is proportional to $\nabla\Phi$, phase singularities represent vortex structures which can drive the motion of detuned neutral atoms by inducing field of mechanical forces [32].

Vortices sometimes display a particlelike behavior, showing attraction and repulsion somewhat similar to point electric charges. Some dynamical laser patterns containing interacting vortices have been discussed in Ref. [29], where a direct integration of a reduced model of the laser equations [28] was performed, and in Ref. [30b], which analyzed the full model of [13]. Vortex motion and interaction is also analyzed in [21]. Space-time chaos in the presence of a large number of vortices has been experimentally observed [20].

In Ref. [17] we considered the case of a narrow atomic gain line capable of selectively exciting the modes of a frequency-degenerate family. Under these conditions, the laser usually approaches stationary states where the various modes of the family lock their phases in appropriate ways. Such stationary states correspond to the local minima of an appropriate generalized free energy [18]. Over extended regions of the parameter space one finds that different stable patterns coexist. This phenomenon, called *spatial optical multistability,* may become useful for applications to optical information processing [17,18]. Stable patterns are characterized by crystalline arrays of optical vortices; as a matter of fact, experimental observations of optical vortices in nonlinear optical systems have been obtained in the form of these crystals [16,17] (an early observation of defects in linear optical systems was reported in [31b]). Comparison between theoretical predictions and experimental findings concerning stationary laser structures can be found in Refs. [17,23].

When the gain line simultaneously excites two or more frequency-degenerate families of modes, the laser usually approaches a dynamical state which may be periodic, quasiperiodic, or chaotic. We will show examples which include cases of rotating patterns and structures displaying creation and annihilation of optical vortices. In fact, under appropriate conditions the nonlinear mode-mode interaction destabilizes the single-mode stationary states, and spontaneously produces coexisting modes which oscillate with different frequencies. In a first approximation, the dynamical behavior appears to arise from the frequency beating of these modes; it must be observed here that, while in the plane-wave theory the mode beating is a simple phenomenon, in the case of transverse modes it can give rise to rather spectacular effects. In addition, the nonlinearity may originate temporal modulations of the mode intensities, and lead to the appearance of further frequencies unrelated to intermode beat frequencies.

In these two papers we report on a correlated theoretical-experimental research work on transverse dynamical phenomena in lasers. The first paper describes the effects predicted by theory, and the second [33] illustrates the observations obtained in two experiments, one using a Na_2 laser and the other a CO_2 laser, and compares experimental data with theoretical predictions. It must be kept in mind, however, that neither theoretical nor experimental results can be considered systematic: the variety of these phenomena seems so vast that what we are attempting here is only an initial classification.

In this paper, Sec. II presents the model we use in our theoretical calculations. Section III contains the linear stability analysis of the single-mode stationary solutions corresponding to the TEM_{00} and TEM_{01}^{*} modes. Section IV gives an extended illustration of several dynamical patterns which arise from the interaction of three or six cavity modes. In particular, in Secs. IV E, IV F, and IV G, we analyze the effects which arise when the cylindrical symmetry of the laser is broken.

II. DESCRIPTION OF THE MODEL

We consider a ring cavity with two spherical mirrors having a radius of curvature R_0 and transmissivity T, and two perfectly reflecting plane mirrors (Fig. 1). The total length of the cavity is $\mathcal{L}$, while L is the distance between the two spherical mirrors, and L_A the length of the active medium, which is assumed to be a homogeneously

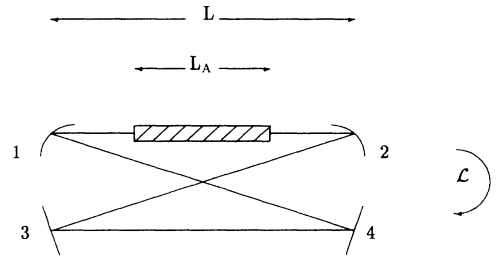

FIG. 1. Scheme of the ring laser. The ring resonator is formed by four mirrors, of which 1 and 2 are spherical mirrors with radius of curvature R_0, reflectivity R, and transmissivity $T=1-R$, while 3 and 4 are perfectly reflecting plane mirrors. $\mathcal{L}$ is the total round trip, L is the distance between the spherical mirrors, and L_A is the length of the active medium.

broadened collection of two-level atoms with transition frequency ω_a and linewidth $\gamma_\perp$; α is the unsaturated gain per unit length experienced by the light passing through the medium.

Our study is based on a suitable expansion of the electric field in terms of the empty cavity modes. In the paraxial approximation, they are solutions of the free field equation

$$\frac{1}{2ik_0}\nabla_\perp^2 A(r,\varphi,z)+\frac{\partial}{\partial z}A(r,\varphi,z)=0\ , \tag{2.1}$$

where $k_0=\omega_0/c$ is the wave vector associated with the reference frequency ω_0, and $\nabla_\perp^2$ is the transverse Laplacian

$$\nabla_\perp^2=\frac{\partial^2}{\partial x^2}+\frac{\partial^2}{\partial y^2}=\frac{\partial^2}{\partial r^2}+\frac{1}{r}\frac{\partial}{\partial r}+\frac{1}{r^2}\frac{\partial^2}{\partial\varphi^2}\ , \tag{2.2}$$

where the second expression holds in cylindrical coordinates that we use in the following, in accord with the symmetry of the system.

The solutions of Eq. (2.1) in the part of the cavity between the two spherical mirrors are the Gauss-Laguerre functions [34]

$$A_{p,l}(r,\varphi,z)=\left[\frac{2}{\pi}\right]^{1/2}\frac{1}{w(z)}\left[\frac{2r^2}{w^2(z)}\right]^{|l|/2}\times L_p^{|l|}\left[\frac{2r^2}{w^2(z)}\right]e^{ik_0r^2/2R(z)}e^{-r^2/w^2(z)}e^{il\varphi}\ , \tag{2.3}$$

where $p=0,1,\ldots$ is the radial index, $l=0,\pm1,\ldots$ is the angular index, $L_p^{|l|}$ are the Laguerre polynomials of the indicated argument, and the functions $w(z)$ and $R(z)$ are defined as

$$w(z)=w_0\left[1+\left[\frac{z}{z_0}\right]^2\right]^{1/2}\ , \tag{2.4}$$

$$R(z)=\frac{z^2+z_0^2}{z}\ . \tag{2.5}$$

The parameter $w_0=w(0)$ is the minimum waist size, while $z_0=k_0w_0^2/2$ is the Rayleigh length of the cavity. Their values are fixed by the geometrical parameters $\mathcal{L}$, L, and R_0 of the cavity, which also determine the eigenfrequencies of the resonator according to the formula

$$w_{n,p,l}=\frac{c}{\mathcal{L}}\left\{2\pi n+2(2p+|l|+1)\cos^{-1}\left[\left[1-\frac{L}{R_0}\right]\left[1-\frac{\mathcal{L}-L}{R_0}\right]\right]^{1/2}\right\}\ , \tag{2.6}$$

where $n=0,1,2\ldots$ is the longitudinal index. An important consequence of Eq. (2.6) is that the frequency of the Gauss-Laguerre modes depends on the transverse indices p and l via the combination $2p+|l|$ only, a situation that produces degeneracy. The modes gather in degenerate families, labeled by the index $q=2p+|l|$ as shown in Fig. 2. In the following we will denote the transverse modes of the cavity by the pair of indices (p,l). The degenerate family of order q consists of $q+1$ modes, and the composition of the first four families is shown in Table I.

In the literature, mode (0,0) is usually designated as TEM_{00}, and modes $(0,\pm l)$ are called TEM_{0l}^* hybrid modes or doughnut modes because they have an annular intensity profile.

The functions $A_{p,l}$ obey, independently of z, the orthonormality relation

$$\int_0^{2\pi}d\varphi\int_0^\infty dr\, rA_{p,l}(r,\varphi,z)A_{p',l'}(r,\varphi,z)=\delta_{p,p'}\delta_{l,l'}\ , \tag{2.7}$$

thus forming a complete set of modes in the transverse plane. Therefore, it is possible to expand the slowly varying envelope of the electric field $F(r,\varphi,z,t)$ in terms of the Gauss-Laguerre functions

$$F(r,\varphi,z,t)=\sum_{p,l}f_{p,l}(z,t)A_{p,l}(r,\varphi,z)\ , \tag{2.8}$$

where the modal amplitudes $f_{p,l}$ are generally complex functions.

At this point we consider some limiting assumptions that allow for a considerable simplification of the analytical description:

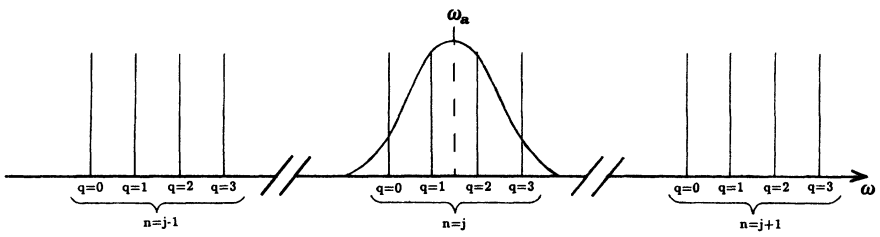

FIG. 2. Spectrum of the eigenfrequencies of the resonator. Three groups of frequencies are shown, corresponding to three adjacent longitudinal indices; q labels the frequency-degenerate family of transverse modes, and ω_a is the atomic transition frequency. The gain line is much smaller than the free spectral range of the cavity.

TABLE I. Composition of the lowest-order families of transverse modes.

q	Modes of the family
0	(0,0)
1	(0,1) (0,−1)
2	(1,0) (0,2) (0,−2)
3	(1,1) (1,−1) (0,3) (0,−3)

$$\gamma_\perp \ll c/\mathcal{L} , \tag{2.9a}$$

$$\omega_{n,0,1}-\omega_{n,0,0} \ll c/\mathcal{L} , \tag{2.9b}$$

$$\alpha L_A \ll 1 , \tag{2.9c}$$

$$T \ll 1 , \tag{2.9d}$$

$$L_A \ll z_0 . \tag{2.9e}$$

The physical meaning of Eqs. (2.9a) and (2.9b) is that only the modes belonging to the longitudinal family nearest to resonance have enough gain to overcome the losses, while no other longitudinal modes play any role in the dynamics (see Fig. 2). Equations (2.9c) and (2.9d) represent the standard uniform field limit which, together with conditions (2.9a) and (2.9b) ensures that the modal amplitudes $f_{p,l}$ become independent of the longitudinal coordinate z. This does not mean that the total field envelope F is uniform along z, because conditions (2.9a)–(2.9d) do not affect the modal functions $A_{p,l}$. However in the limit (2.9e), the Gauss-Laguerre functions can be considered independent of z inside the atomic sample, where they take the simple form

$$A_{p,l}(\rho,\varphi)=\left[\frac{2}{\pi}\right]^{1/2}(2\rho^2)^{|l|/2}L_p^{|l|}(2\rho^2)e^{-\rho^2}e^{il\varphi} , \tag{2.10}$$

where ρ is the radial coordinate normalized to the beam waist w_0. Of course the orthonormality relation (2.7) is still valid, provided r is substituted by ρ.

We note that, as a consequence of Eqs. (2.9), the field envelope in the atomic sample is independent of z; we can then replace the expansion (2.8) with

$$F(\rho,\varphi,t)=\sum_{p,l} f_{p,l}(t)\,A_{p,l}(\rho,\varphi) . \tag{2.11}$$

Upon inclusion of this expansion in the Maxwell equation for the electric field interacting with the atomic medium and projecting on the modal eigenfunctions, one finds that the modal amplitudes obey the dynamical equations [13]

$$\frac{df_{p,l}}{dt}=-k\left[(1+ia_{p,l})f_{p,l} - 2C\int_0^{2\pi}d\varphi\int_0^{\infty}d\rho\,\rho\,A^*_{p,l}(\rho,\varphi)P(\rho,\varphi,t)\right] , \tag{2.12a}$$

where $C=\alpha L_A/2T$ is the pump parameter, and $k=cT/\mathcal{L}$ is the cavity linewidth; $a_{p,l}$ denotes the difference between the frequency of the mode of indices p,l and that of the fundamental TEM_{00} mode, normalized to k. P is the normalized slowly varying envelope of the atomic polarization. Equation (2.12a) is coupled to the atomic Bloch equations, which read as

$$\frac{\partial P}{\partial t}=\gamma_\perp[F(\rho,\varphi,t)D(\rho,\varphi,t)-(1+i\delta_{AC})P(\rho,\varphi,t)] , \tag{2.12b}$$

$$\frac{\partial D}{\partial t}=-\gamma_\parallel[\,\mathrm{Re}(F^*(\rho,\varphi,t)P(\rho,\varphi,t))+D(\rho,\varphi,t)-\chi(\rho)] , \tag{2.12c}$$

where D is the normalized population inversion, $\gamma_\parallel$ is its relaxation rate, and δ_{AC} is the detuning of the atomic transition from the frequency of the TEM_{00} mode, normalized to $\gamma_\perp$.

The function $\chi(\rho)$ describes the transverse configuration of the population inversion at equilibrium due to the pumping. We have chosen a Gaussian profile of width r_p,

$$\chi(\rho)=\exp(-2\rho^2/\psi^2), \quad \psi=2r_p/w_0 , \tag{2.13}$$

suitable, among other things, to describe optical pumping, r_p being the width of the pump laser.

We point out that in expansion (2.11) one should consider *a priori* all the modal amplitudes $f_{p,l}$, with $p=0,1,\ldots$, and $l=0,\pm1,\ldots$. However, in the majority of real devices, transverse modes with large values of the indices p and l suffer from higher losses as a result of the finite size of the mirrors, the limited diameter of the active medium, and the presence of intracavity elements such as pinholes, modulators, etc. Hence only the lowest transverse modes are usually involved in the dynamics, and we shall limit our considerations to a reasonably small number of modal families. As a matter of fact, the modal equations (2.12a) are useful only as long as a reasonably limited number of modes is involved; otherwise, it is more convenient to solve directly the partial differential equation for the field envelope, which is equivalent to the set of ordinary integrodifferential modal equations (2.12a) [see Eq. (2.37) in Refs. [13] and [23]].

The larger losses of higher-order modes might be taken into account by including in Eqs. (2.12a) a loss parameter which depends on the modal indices p and l, as is done, for example, in Ref. [23]. However, in this paper, we will not follow this procedure, with the exception of Sec. IV F; we will consider only cases in which the dynamics of the system is governed by two ($q=0,1$) or three ($q=0,1,2$) families of modes, with the aim of describing the simplest step of pattern formation in lasers. In our calculations, based on the modal equations (2.12), we have checked that the inclusion of higher-order families does not affect the result appreciably, because the amplitudes of the modes of the higher-order families are negligible. We end this section with two remarks.

(1) When frequency spacings among the relevant modes are of the order of the cavity linewidth k, the modes tend to lock because of the mechanism of "cooperative frequency locking" [10,13,14]. In this case

the laser approaches a stationary state, because the state displays a single oscillation frequency. When, on the other hand, the frequency spacings are substantially larger than k, the laser usually approaches a dynamical state characterized by one or more additional frequencies. Even in this case, however, modes with the same value of the angular index l show a tendency to lock and oscillate with the same frequency; we noted this phenomenon both in the theoretical and experimental observations. This phenomenon is similar to that described by Lin and Abraham [35], and can be interpreted as the result of the fact that a given spatial structure of the beam oscillating at a single frequency cannot in general be described by a single cavity mode. Thus an ensemble of modes with a compatible angular distribution of the field becomes necessary in order to take into account the influence introduced by the medium on the final solution.

(2) The case described by Fig. 2 is that of a cavity near to (or not too distant from) a configuration of plane mirrors. In this situation the quantities $a_{p,l}$ in Eqs. (2.12a) are positive. Another case, which can still be described by Eqs. (2.12a), is that of a cavity close to a concentric configuration; in this situation the parameters $a_{p,l}$ are negative. All the results obtained for the quasiplanar case hold also for the quasiconcentric configuration, because a simultaneous change of sign of $a_{p,l}$ and δ_{AC} does not change the physical situation.

III. STABILITY ANALYSIS OF SINGLE-MODE STATIONARY SOLUTIONS

By appropriately choosing the atomic linewidth and the frequency spacing between adjacent families of transverse modes we can realize a situation where only modes belonging to families $q=0$ and 1 can take part in the lasing process. They are described by the following functions:

$$A_1(\rho)=A_{0,0}(\rho)=\left[\frac{2}{\pi}\right]^{1/2}e^{-\rho^2}, \tag{3.1}$$

$$A_2(\rho,\varphi)=A_{0,1}(\rho,\varphi)=\frac{2}{\sqrt{\pi}}\rho e^{-\rho^2}e^{i\varphi}, \tag{3.2}$$

$$A_3(\rho,\varphi)=A_{0,-1}(\rho,\varphi)=\frac{2}{\sqrt{\pi}}\rho e^{-\rho^2}e^{-i\varphi}, \tag{3.3}$$

so that the electric field is

$$F(\rho,\varphi,t)=\sum_{i=1}^{3}f_i(t)A_i(\rho,\varphi). \tag{3.4}$$

With this limitation one can guarantee the existence of single-mode stationary solutions. There are obviously three such solutions: one is the TEM_{00} solution, and the other two are doughnuts with left and right helicities; the last two prove to be perfectly equivalent from the points of view of the steady state and the linear stability analysis.

In the following subsections we will study the stability of the two classes of single-mode solutions (TEM_{00} in Sec. III A and doughnuts in Sec. III B) against fluctuations of the modes of the other family (doughnuts in Sec. III A and TEM_{00} in Sec. III B). As for dynamical regimes involving higher-order families ($q=2,3,\ldots$) results can be obtained only by numerical integration of the equations (see Secs. IV D and IV H).

A. Destabilization of the TEM_{00} single-mode steady state

The TEM_{00} stationary solution is found by setting $f_2=f_3=0$ in Eqs. (2.12a)–(2.12c), and assuming

$$f_1=f_1^{st}\exp(-ik\Delta t),\quad P=P^{st}(\rho,\varphi)\exp(-ik\Delta t),$$
$$D=D^{st}(\rho,\varphi),$$

where $k\Delta$ accounts for the mode pulling. The single-mode steady-state equation is then

$$1=2C\int_0^\infty d\rho\,4\rho\frac{e^{-2\rho^2}}{1+\Delta^2+e^{-2\rho^2}x_1^2}\chi(\rho), \tag{3.5}$$

where

$$x_1=\left[\frac{2}{\pi}\right]^{1/2}|f_1^{st}| \tag{3.6}$$

and

$$\Delta=\frac{\delta_{AC}}{1+\tilde{k}},\quad \tilde{k}=\frac{k}{\gamma_\perp}. \tag{3.7}$$

The threshold for laser emission can be obtained by setting $x_1=0$ in Eq. (3.5):

$$2C_{(0,0)}^{thr}=(1+\Delta^2)\frac{\psi^2+1}{\psi^2}, \tag{3.8}$$

that in the limit of flat pump profile $\psi\to\infty$ reduces to the usual expression of the plane-wave theory. The expressions of $P^{st}(\rho)$ and $D^{st}(\rho)$ are

$$P^{st}(\rho)=\frac{(1-i\Delta)\chi(\rho)F^{st}(\rho)}{1+\Delta^2+|F^{st}(\rho)|^2},$$
$$D^{st}(\rho)=\frac{(1+\Delta^2)\chi(\rho)}{1+\Delta^2+|F^{st}(\rho)|^2}, \tag{3.9}$$

where $F^{st}(\rho)$ is given by Eq. (3.4) with $f_2=f_3=0$, and $f_1(t)$ replaced by f_1^{st}. In order to study the stability of the TEM_{00} single-mode stationary solution, we introduce in Eqs. (2.12) the change of variables

$$\bar{f}_i(t)=f_i(t)\exp(ik\Delta t),$$
$$\bar{P}(\rho,\varphi,t)=P(\rho,\varphi,t)\exp(ik\Delta t),$$
$$\bar{D}(\rho,\varphi,t)=D(\rho,\varphi,t), \tag{3.10}$$

we consider a small perturbation

$$\delta f_1(t)=\bar{f}_1(t)-f_1^{st},$$
$$\delta f_i(t)=\bar{f}_i(t)\quad (i=2,3),$$
$$\delta P(\rho,\varphi,t)=\bar{P}(\rho,\varphi,t)-P^{st}(\rho),$$
$$\delta D(\rho,\varphi,t)=\bar{D}(\rho,\varphi,t)-D^{st}(\rho), \tag{3.11}$$

and we linearize the dynamical equations around the

steady state. Then we introduce the exponential ansatz

$$\begin{bmatrix} \delta f_i(t) \\ \delta f_i^*(t) \\ \delta P(\rho,\varphi,t) \\ \delta P^*(\rho,\varphi,t) \\ \delta D(\rho,\varphi,t) \end{bmatrix} = e^{\tilde{\lambda}\gamma_\perp t} \begin{bmatrix} \delta f_i^0 \\ \delta f_i^{0*} \\ \delta P^0(\rho,\varphi) \\ \delta P^{0*}(\rho,\varphi) \\ \delta D^0(\rho,\varphi) \end{bmatrix} , \tag{3.12}$$

and obtain two closed sets of linear equations for the variables δf_1^0 and δf_1^{0*}, and for the variables δf_2^0, δf_2^{0*}, δf_3^0, and δf_3^{0*}. Only the latter set can produce an instability, and it leads to the following secular equation in $\tilde{\lambda}$:

$$[\tilde{\lambda}+i\eta+\tilde{k}(1-2C\Phi-i\Delta)][\tilde{\lambda}-i\eta+\tilde{k}(1-2C\Phi^\dagger+i\Delta)] -4C^2\tilde{k}^2\Psi\Psi^\dagger x_1^4=0 , \tag{3.13}$$

where

$$\eta=\frac{\omega_{n,0,1}-\omega_{n,0,0}}{\gamma_\perp} , \tag{3.14}$$

and the $\dagger$ operation corresponds to a complex conjugation which, however, leaves $\tilde{\lambda}$ unchanged; the function Φ and Ψ are defined by

$$\Phi(|F^{\rm st}|^2,\tilde{\gamma},\Delta,\tilde{\lambda})=\int_0^\infty d\rho\, 8\rho^3 e^{-2\rho^2} T_1(|F^{\rm st}|^2,\tilde{\gamma},\Delta,\tilde{\lambda})\chi(\rho) , \tag{3.15}$$

$$\Psi(|F^{\rm st}|^2,\tilde{\gamma},\Delta,\tilde{\lambda})=\int_0^\infty d\rho\, 8\rho^3 e^{-4\rho^2} T_2(|F^{\rm st}|^2,\tilde{\gamma},\Delta,\tilde{\lambda})\chi(\rho) , \tag{3.16}$$

with

$$\tilde{\gamma}=\gamma_\parallel/\gamma_\perp , \tag{3.17}$$

$$T_1(|F^{\rm st}|^2,\tilde{\gamma},\Delta,\tilde{\lambda})=\frac{2(1+\Delta^2)(\tilde{\gamma}+\tilde{\lambda})(1+\tilde{\lambda}-i\Delta)-\tilde{\gamma}\tilde{\lambda}(1+i\Delta)|F^{\rm st}|^2}{2(1+\Delta^2+|F^{\rm st}|^2)\{(\tilde{\gamma}+\tilde{\lambda})[(1+\tilde{\lambda})^2+\Delta^2]+\tilde{\gamma}(1+\tilde{\lambda})|F^{\rm st}|^2\}} , \tag{3.18}$$

and

$$T_2(|F^{\rm st}|^2,\tilde{\gamma},\Delta,\tilde{\lambda})=\frac{\tilde{\gamma}(\tilde{\lambda}+2)(-1+i\Delta)}{2(1+\Delta^2+|F^{\rm st}|^2)\{(\tilde{\gamma}+\tilde{\lambda})[(1+\tilde{\lambda})^2+\Delta^2]+\tilde{\gamma}(1+\tilde{\lambda})|F^{\rm st}|^2\}} , \tag{3.19}$$

where

$$|F^{\rm st}|^2=|f_1^{\rm st}|^2|A_1(\rho)|^2=x_1^2 e^{-2\rho^2} . \tag{3.20}$$

The single-mode stationary solution corresponding to the TEM_{00} mode becomes unstable when Eq. (3.13) admits a solution with a positive real part. As usual, in the parameter space of the system there are two kinds of boundaries for the stability domain. The first type is characterized by the fact that a real eigenvalues changes from negative to positive when the boundary is crossed; in this case one has a steady-state bifurcation. The second type is characterized by the fact that the real part of a pair of complex conjugate eigenvalues changes sign when the boundary is crossed; in this case one has a Hopf bifurcation. Because the boundary of steady-state bifurcation occurs usually for small values of η, such that the validity of the three-mode picture fails because higher-order modes are relevant for the dynamics, in the following we will discuss exclusively the boundary of Hopf bifurcation.

We have been able to solve Eq. (3.13) numerically to any desired level of precision by using coupled Romberg, Newton, and downhill simplex methods [36]. The boundary of the domain of stability in the parameter plane $(2C,\eta)$ for fixed values of ψ, Δ, $\tilde{k}$, and $\tilde{\gamma}$ corresponding to laser cases analyzed in Sec. IV are presented in Figs. (3a)–(3c). Above the solid line the single-mode solution is stable, while below it any fluctuation of modes 2 and 3 grows from noise and destabilizes the TEM_{00} configuration.

In order to gain a better understanding about the terms of Eq. (3.13) which lead to the instability of the Gaussian mode, we have found approximate solutions of this equation in a perturbative way whenever large differences between the decay time scales of the variables occur. We write $\tilde{\lambda}$ as a power series of a small parameter ϵ:

$$\tilde{\lambda}=\tilde{\lambda}_0+\epsilon\tilde{\lambda}_1+\epsilon^2\tilde{\lambda}_2+\cdots , \tag{3.21}$$

and take only the relevant terms in the expansion.

In the good-cavity limit $k\ll\gamma_\perp,\gamma_\parallel$, for example, it is natural to choose $\epsilon=\tilde{k}=k/\gamma_\perp$, (with $\tilde{\gamma}\simeq\epsilon^0$, $\eta\simeq\epsilon^0$); one then obtains

$$\tilde{\lambda}_0=-i\eta , \tag{3.22a}$$

$$\tilde{\lambda}_1=2C\Phi(x_1^2 e^{-2\rho^2},\tilde{\gamma},\delta_{\rm AC},\tilde{\lambda}=\tilde{\lambda}_0)-1+i\delta_{\rm AC} , \tag{3.22b}$$

and the complex conjugate solution; the function Φ is defined by expression (3.15).

Another reasonable choice of the smallness parameter ϵ is possible when $\gamma_\parallel\ll\gamma_\perp$ (with $\tilde{k}\simeq\epsilon^0,\eta\simeq\epsilon^0$), as occurs, for example, in CO_2 and the Nd:YAG (yttrium aluminum garnet) laser; in this case it is convenient to set $\epsilon=\tilde{\gamma}=\gamma_\parallel/\gamma_\perp$, so that the first terms of the series expansion for $\tilde{\lambda}$ are given by

$$\tilde{\lambda}_0=\tfrac{1}{2}\{-[1+i\Delta+i\eta+\tilde{k}(1-i\Delta)] \pm\sqrt{[1+i\Delta-i\eta-\tilde{k}(1-i\Delta)]^2+8C\tilde{k}(1+\Delta^2)I_1}\} , \tag{3.23a}$$

$$\tilde{\lambda}_1=-\frac{2C\tilde{k}(1+i\Delta)(\tilde{\lambda}_0+2)I_2}{2\tilde{\lambda}_0[(1+\tilde{\lambda}_0+i\Delta)^2+2C\tilde{k}(1+\Delta^2)I_1]} , \tag{3.23b}$$

where

$$I_1=\int_0^\infty d\rho\, 4\rho\frac{2\rho^2 e^{-2\rho^2}\chi(\rho)}{1+\Delta^2+x_1^2 e^{-2\rho^2}}$$

and (3.24)

$$I_2=\int_0^\infty d\rho\, 4\rho\frac{2\rho^2 e^{-4\rho^2}\chi(\rho)}{1+\Delta^2+x_1^2 e^{-2\rho^2}}x_1^2$$

and by the complex conjugate solutions. The short (long) dashed lines in Figs. 3(a)–3(c) (when visible), represent the results of the perturbative expansion (3.22) [(3.23)]. Excellent agreement with the full stability analysis (3.13) is found whenever the smallness conditions are verified [in Figs. 3(b) and 3(c), the exact solution is not distinguishable from approximation (3.23)].

B. Destabilization of the doughnut single-mode steady state

In this case the single-mode steady-state equation, obtained by setting $f_1=f_3=0$ in Eqs. (2.12a)–(2.12c), and assuming $f_2=f_2^{\rm st}\exp(-ik\Delta' t)$, $P=P^{\rm st}(\rho,\varphi)\times\exp(-ik\Delta' t)$, and $D=D^{\rm st}(\rho,\varphi)$, is

$$1=2C\int_0^\infty d\rho\, 4\rho\frac{2\rho^2 e^{-2\rho^2}}{1+\Delta'^2+2\rho^2 e^{-2\rho^2}x_2^2}\chi(\rho)\ , \qquad (3.25)$$

where

$$x_2=\left[\frac{2}{\pi}\right]^{1/2}|f_2^{\rm st}| \qquad (3.26)$$

and

$$\Delta'=\Delta-\frac{\eta}{1+\tilde{k}}=\frac{\delta_{\rm AC}-\eta}{1+\tilde{k}}\ . \qquad (3.27)$$

The threshold for laser emission now is [$x_2=0$ in Eq. (3.25)]

$$2C^{\rm thr}_{(0,\pm1)}=(1+\Delta'^2)\left[\frac{\psi^2+1}{\psi^2}\right]^2 . \qquad (3.28)$$

We now consider the field fluctuations to be

$$\delta f_2(t)=\bar{f}_2(t)-f_2^{\rm st}\ ,$$
$$\delta f_i(t)=\bar{f}_i(t)\quad (i=1,3)\ , \qquad (3.29)$$

where $\bar{f}_i(t)$ is defined as in Eq. (3.10), with Δ replaced by $\Delta'+\eta/\tilde{k}$. We then retrace all the steps followed in Sec. III A, and we arrive at the expression for the characteristic equation in $\tilde{\lambda}$ which governs the stability of the single-mode doughnut solution against the growth of the TEM_{00} mode:

$$\tilde{\lambda}-i\eta+\tilde{k}(1-2C\Phi'-i\Delta')=0\ , \qquad (3.30)$$

where

$$\Phi'(|F^{\rm st}|^2,\tilde{\gamma},\Delta',\tilde{\lambda})=\int_0^\infty d\rho\, 4\rho e^{-2\rho^2}T_1(|F^{\rm st}|^2,\tilde{\gamma},\Delta',\tilde{\lambda})\chi(\rho) \qquad (3.31)$$

and

$$|F^{\rm st}|^2=|f_2^{\rm st}|^2|A_2(\rho,\varphi)|^2=x_2^2 2\rho^2 e^{-2\rho^2}\ . \qquad (3.32)$$

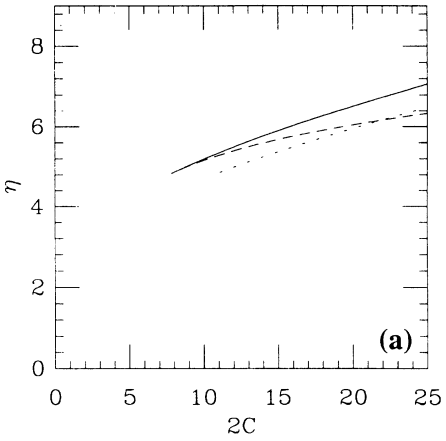

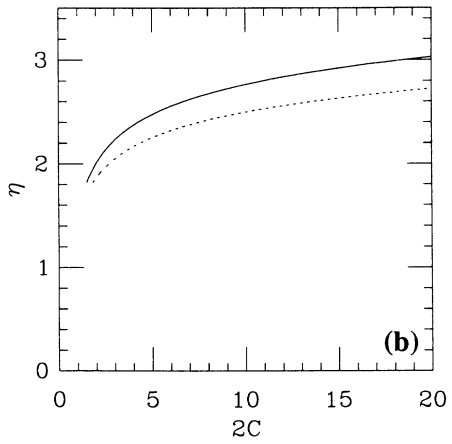

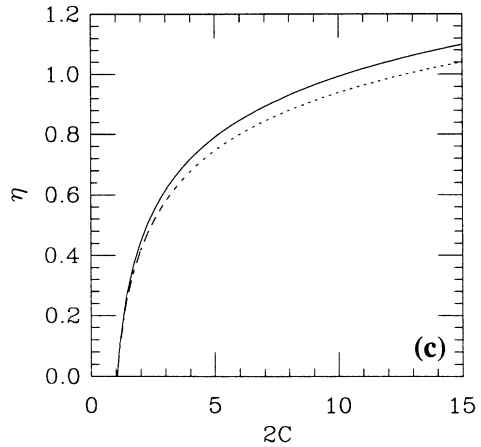

FIG. 3. Stability boundaries for the TEM_{00} mode for the different parameter regions considered in this paper. This mode is unstable below these curves and stable above them. The solid lines indicate the exact numerical solution of Eq. (3.13). The approximate solutions are indicated by dashed lines when not hidden by the solid line (short dashes for the good cavity limit [Eqs. (3.22)], and longer dashes for the small-$\tilde{\gamma}$ limit [Eqs. (3.23)]). (a) Na_2 laser parameters ($\tilde{k}=0.23$, $\tilde{\gamma}=1$, $\Delta=2.16$, and $\psi=1.63$). (b) CO_2 parameters ($\tilde{k}=0.3$, $\tilde{\gamma}=0.01$, $\Delta=0.7$, and $\psi\to\infty$). (c) Nd:YAG parameters ($\tilde{k}=0.05$, $\tilde{\gamma}=0.0025$, $\Delta=-0.2$, and $\psi\to\infty$).

In this case we have not evaluated the exact solutions of Eq. (3.30), limiting ourselves to the analysis of the perturbative cases $\tilde{k} \ll 1$ and $\tilde{\gamma} \ll 1$ with the same approach as in Sec. III A. In the good-cavity limit we have

$$\tilde{\lambda}_0 = +i\eta \ , \tag{3.33a}$$

$$\tilde{\lambda}_1 = 2C\Phi'(|F^{\mathrm{st}}|^2, \tilde{\gamma}, \delta_{\mathrm{AC}} - \eta, \tilde{\lambda} = \tilde{\lambda}_0) - 1 + i(\delta_{\mathrm{AC}} - \eta) \ , \tag{3.33b}$$

and the complex conjugate solution.

In the second limit one has

$$\tilde{\lambda}_0 = \tfrac{1}{2}\{ -[1 + i\Delta' - i\eta + \tilde{k}(1 - i\Delta')] \pm \sqrt{[1 + i\Delta' + i\eta - \tilde{k}(1 - i\Delta')]^2 + 8C\tilde{k}(1 + \Delta'^2) I_3} \}, \tag{3.34a}$$

$$\tilde{\lambda}_1 = -\frac{2C\tilde{k}(1 + i\Delta')(\tilde{\lambda}_0 + 2) I_4}{2\tilde{\lambda}_0[(1 + \tilde{\lambda}_0 + i\Delta')^2 + 2C\tilde{k}(1 + \Delta'^2) I_3]} \ , \tag{3.34b}$$

where

$$I_3 = \int_0^\infty d\rho \, 4\rho \frac{e^{-2\rho^2} \chi(\rho)}{1 + \Delta'^2 + x_2^2 2\rho^2 e^{-2\rho^2}} \tag{3.35a}$$

and

$$I_4 = \int_0^\infty d\rho \, 4\rho \frac{2\rho^2 e^{-4\rho^2} \chi(\rho)}{1 + \Delta'^2 + x_2^2 2\rho^2 e^{-2\rho^2}} x_2^2 \ , \tag{3.35b}$$

together with the complex conjugate solution.

Figures 4(a)–4(c) display the various regions of stability as provided by the two stability analyses described in this section and Sec. III A in the limit $\tilde{k} \ll 1$ for Fig.

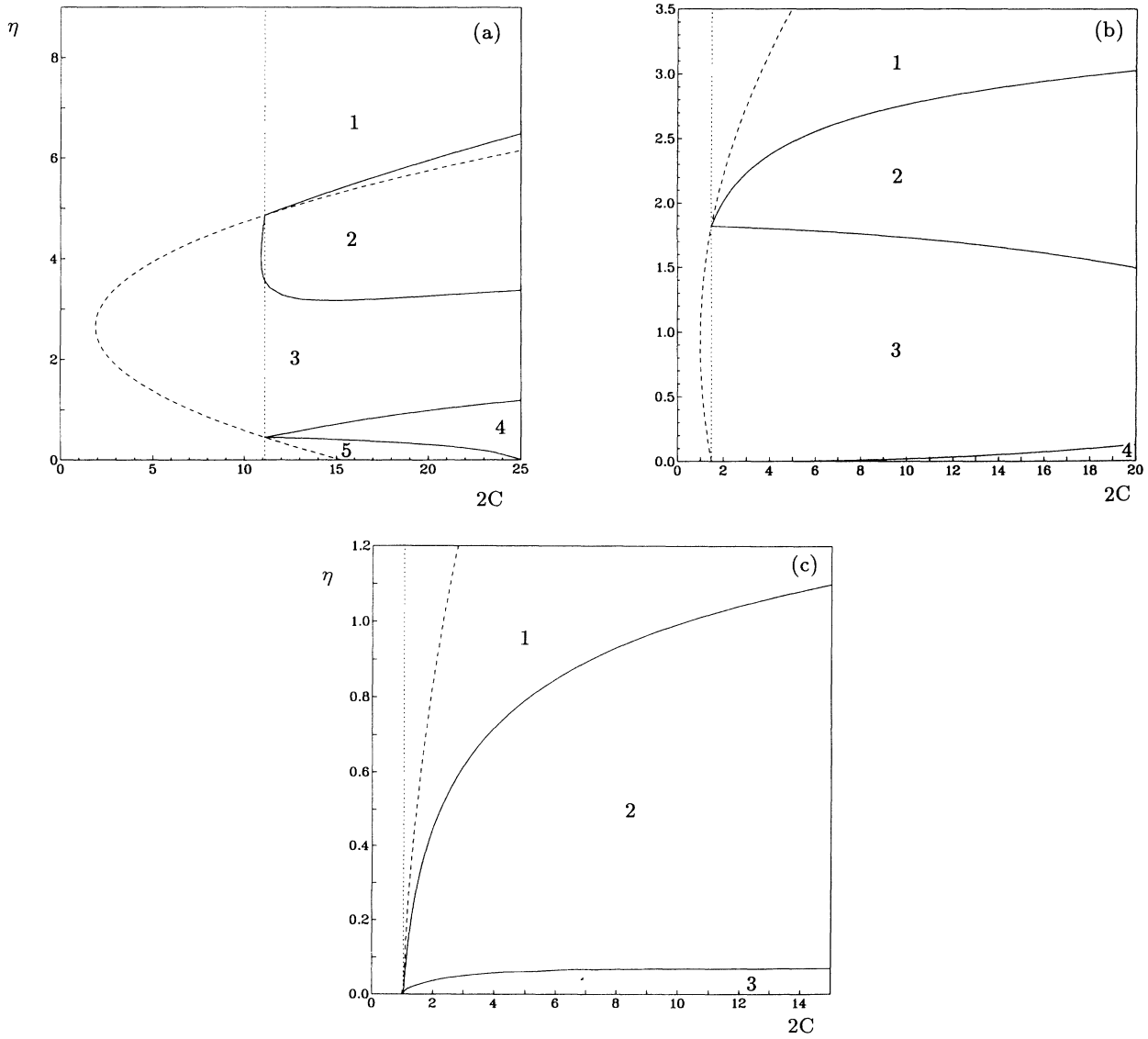

FIG. 4. Stability boundaries of the TEM_{00} and $(0, \pm 1)$ single-mode solution. (a) Parameters as in Fig. 3(a). (b) Parameters as in Fig. 3(b). (c) Parameters as in Fig. 3(c). Regions 1 in (a)–(c) and 5 in (a) lie on the right of the vertical dotted line, while region 3 in (a) and (b) lies on the right of the dashed line; all regions are separated by the solid lines.

4(a), and $\tilde{\gamma} \ll 1$ for Figs. 4(b) and 4(c); the other parameters are equal to those used in Figs. 3(a), 3(b), and 3(c), respectively. In these figures the dotted line represents the threshold of the TEM_{00} single-mode solution, while the dashed line shows the threshold for the doughnut solutions. In Fig. 4(a), upon decreasing the mode spacing η one encounters in order (1) region 1, where only the TEM_{00} solution exists and is stable; (2) region 2, where the TEM_{00} solution is unstable, and the doughnut solutions either do not exist (above the dashed line) or are unstable; (3) region 3, where only the doughnut solutions are stable, (4) region 4, where both the TEM_{00} and the doughnut solutions are stable; and, finally, (5) region 5, where only the TEM_{00} solution is stable. In Fig. 4(b), regions 1, 2, and 3 are characterized by the same stability scenery as in Fig. 4(a), and region 4 presents the same stability picture as region 2. In Fig. 4(c) the scenery is the same as in Fig. 4(b), but there is no equivalent of region 4.

The dynamics of the multimode patterns that arise when both TEM_{00} and the doughnut solutions become unstable will be the subject of Sec. IV. The search for dynamical laser solutions has been guided by the diagrams of Figs. 3 and 4.

IV. NUMERICAL ANALYSIS OF DYNAMICAL INSTABILITIES

In this section we present some results of extensive investigation of the dynamical regimes obtained by integration of Eqs. (2.12). Note that the sign of the atomic detuning Δ is positive (i.e., the atomic frequency is larger than the Gaussian mode frequency, which corresponds to self-focusing in the laser case) for some simulations and negative for others, without substantial differences in the spatiotemporal behavior of the laser output (apart from mode family selection with $\Delta > 0$), in agreement with the experimental results. This may appear to contrast recent work [37], which shows pinned singularities for $\Delta > 0$ and free vortices for $\Delta < 0$ in a laser model with plane mirrors and an infinitely extended pump. The presence of spherical mirrors and a finite-size pump induces a mechanism that binds vortices for all signs of detuning, as clearly explained in Ref. [29]. Moreover, for positive detunings, pinned phase singularities in equations (2.12) have been already described in Ref. [17] as the single degenerate family effect. Here we focus on the dynamics of laser vortices when more than one family of modes is active. In these cases the bound motions of vortices for positive and negative detunings appear indistinguishable.

A. Dynamical patterns in the case of a frequency-degenerate family

When the dynamics is governed only by the modes of a frequency-degenerate family, usually the laser approaches a stationary state. This is always true in the good-cavity limit $k \ll \gamma_\perp, \gamma_\parallel$, in which the atomic variables can be eliminated adiabatically, and the equations which describe the behavior of the system can be cast in a "potential" form [18]; it is, however, not true for general values of the relaxation rates k, $\gamma_\perp$, and $\gamma_\parallel$. As a matter of fact our investigations in the parameter domain proper for CO_2 lasers, and our attempts to forecast relaxation oscillations in the crystals of phase singularities [17], led us to regimes where spontaneous oscillations of the modal intensities belonging to the same frequency-degenerate family set in, so that the system reaches a dynamical steady state which we always found to be a limit cycle.

The parameter domain where this behavior can be found is characterized by a small $\tilde{\gamma}$ [see Eq. (3.17)], usually around 10^{-2}, while the cavity damping constant $\tilde{k}$ can vary from 10^{-1} to unity. The pump parameter ranges from values very close to threshold to a few times above threshold; beyond this limit the system switches back to a stationary steady state. The pump profile has always been kept flat ($\psi \to \infty$).

An example of the oscillatory regime is reported in Fig. 5: here we have considered the family $q=2$ to be active, and as an initial condition we chose a four-hole pattern, similar to that described in Fig. 6(b) of Ref. [17]. For $\tilde{\gamma} \geq 0.05$ this pattern is a stable stationary state for the system, but we have numerically integrated the model with $\tilde{\gamma}=0.01$, and the onset of the oscillations is quite clear. As one can see, the intensity of mode $A_{1,0}$ is larger than those of modes $A_{0,\pm 2}$, it oscillates with half the period of the oscillations of those modes with a smaller amplitude. Moreover, mode $A_{0,+2}$ is in counterphase to $A_{0,-2}$, and has the same amplitude of oscillation. This behavior is very similar to the antiphase dynamics recently studied by many authors [38], and it is common to all the dynamical regimes we found all over the parametric region investigated. It is worth stressing that the same regime is reached under fixed parametric conditions, independently of the initial conditions, i.e., there is no evi-

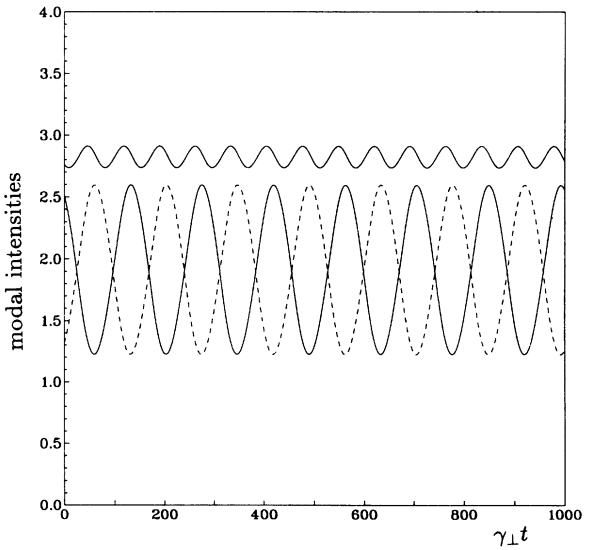

FIG. 5. Spontaneous oscillations of the frequency-degenerate family $q=2$ for $\tilde{\gamma}=0.01$. $\psi \to \infty$, $2C=2$, and $\tilde{k}=1$. Time evolution of the modal intensities. The upper solid line represents the mode (1,0), and the two lower lines show antiphase oscillations of the doughnut modes (0,+2) (solid line) and (0,−2) (broken line).

dence of multistability, in contrast to the good-cavity case.

There are always four vortices in this dynamical pattern, which move around the optical axis, and at the same time oscillate along the radial direction: Figure 6 illustrates this motion in the transverse plane during 200 times units; note that the orbits of the vortices are quasi-periodic due to the relations among modal amplitude oscillations and their phases.

We compared the numerically calculated oscillation frequencies to the relaxation oscillation frequency predicted by the plane-wave rate equation model for a class-*B* laser:

$$\frac{\omega}{\gamma_\perp}=\sqrt{2\tilde{k}\tilde{\gamma}(2C-1)-(C\tilde{\gamma})^2}\ . \tag{4.1}$$

As one can see from Fig. 7, full agreement cannot be attained, but the numerical values are satisfactorily centered around the theoretical curves; this agreement tends to be lost for high values of C and $\tilde{k}$.

As the ratio $\tilde{\gamma}/\tilde{k}$ is further decreased to values of the order of 10^{-3}, the behavior of the system becomes simpler because the antiphase oscillations disappear. The modal intensities $|f_{0,1}|^2$, $|f_{0,2}|^2$, and $|f_{0,-2}|^2$ are constant and $|f_{0,2}|=|f_{0,-2}|$, but the phases of the doughnut amplitudes $f_{0,2}$ and $f_{0,-2}$ rotate at the same frequency ω and in opposite directions, i.e., $f_{0,2}=|f_{0,2}|e^{-i\omega t}$, and $f_{0,-2}=|f_{0,-2}|e^{i\omega t}$. Consequently, the four phase singularities will rotate about the optical axis at the frequency ω, but the radial motion disappears. In this limit it is possible to derive more precise formulas for the modal intensities $x_1=|f_{0,1}|^2$ and $x_2=|f_{0,2}|^2$ and for the rotation frequency ω:

$$1=2C\int_0^\infty du\frac{(1-u)^2e^{-u}\chi}{1+[(1-u)^2x_1+u^2x_2]e^{-u}}\ , \tag{4.2a}$$

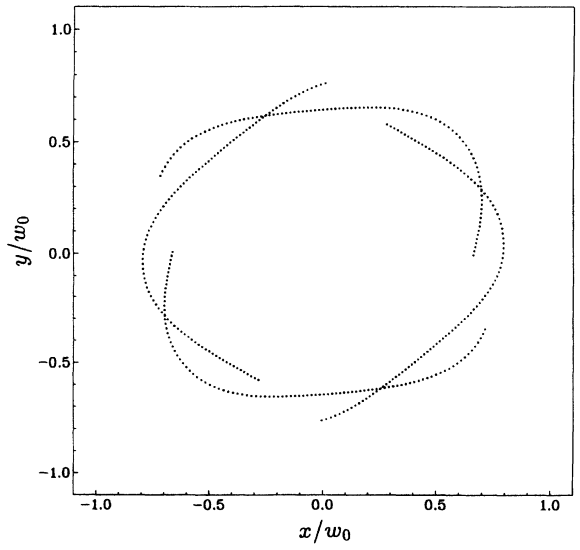

FIG. 6. Motion of the four vortices in the (x,y) transverse plane for the dynamical regime of Fig. 5.

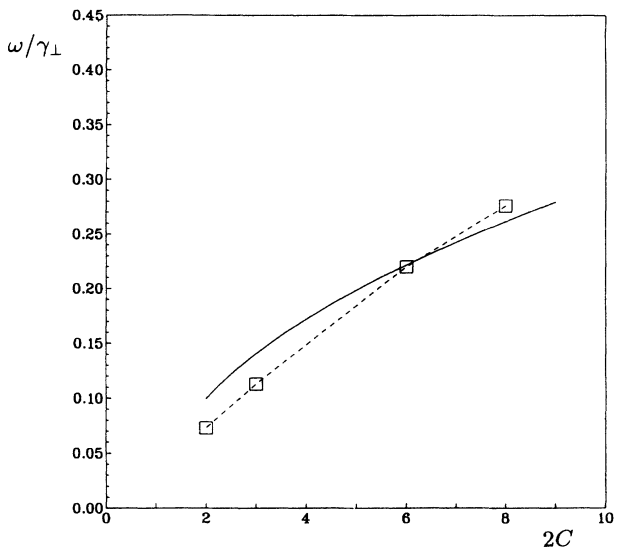

FIG. 7. Comparison between the numerically calculated frequency for the oscillations of the regime corresponding to Fig. 5 (squares), with $\tilde{\gamma}/\tilde{k}=0.02$, and the theoretical frequency for relaxation oscillations in class *B* lasers (solid line).

$$1=2C\int_0^\infty du\frac{u^2/2e^{-u}\chi}{1+[(1-u)^2x_1+u^2x_2]e^{-u}}\ , \tag{4.2b}$$

$$\left[\frac{\omega}{k}\right]^2=2C\frac{\tilde{\gamma}}{\tilde{k}}\frac{x_2}{8}\int_0^\infty du\frac{u^4e^{-2u}\chi}{1+[(1-u)^2x_1+u^2x_2]e^{-u}}\ . \tag{4.2c}$$

By substituting the values for the intensities x_1 and x_2 obtained from the first two equations in the last equation, one obtains the rotation frequency ω as a function of the pump parameter $2C$. Figure 8 shows the perfect agreement between the theoretical curve and the numerical values derived by integration of the dynamical equations.

B. Three-mode laser: Na_2 parameters, traveling wave

In this subsection and the following one, we consider physical conditions in which the laser line excites only the three modes where $q=0$ and 1. The estimated values for the relaxation rates in the experiment with the Na_2 laser described in paper II are $\tilde{k}=0.23$ and $\tilde{\gamma}=1$. The other parameters are not fixed. We have gradually decreased η [Eq. (3.14)] crossing the instability threshold. Below the boundary curve given by the solid line in Fig. 3(a) [or by the line which separates regions 1 and 2 in Fig. 4(a)], we have observed the emergence of a rotating pattern characterized by the presence of just one component of the TEM_{00} mode, and one of the $(0,\pm1)$ modes. The intensities $|f_i|^2$ of the modal components are constant, while the relative phase increases (or decreases) linearly with time, and the rate of increase (decrease) is equal to the mode-pulled frequency spacing between the two modes:

$$\delta\omega=\frac{\eta}{1+\tilde{k}}\gamma_\perp\ . \tag{4.3}$$

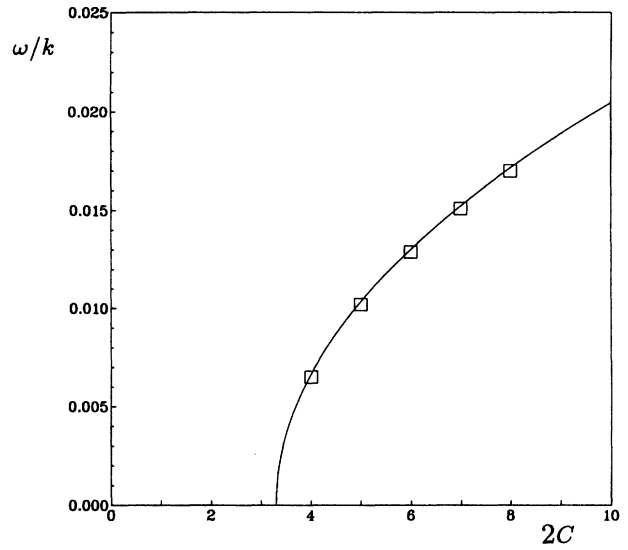

FIG. 8. Same as Fig. 7, except that $\bar{\gamma}/\tilde{k}=10^{-3}$ and the numerical values of the rotation frequency (squares) are compared with the theoretical curve obtained from Eqs. (4.2).

Let us consider, for example, the case in which mode $(0,-1)$ is activated; using the same modal amplitudes f_i $(i=1,2,3)$ as in Sec. III, the intensity profile of this pattern has the form

$$|F(\rho,\varphi,t)|^2=\frac{2}{\pi}e^{-2\rho^2}|f_1^0+\sqrt{2}\rho f_3^0 e^{-i(\varphi+\delta\omega t)}|^2$$
$$=\frac{2}{\pi}e^{-2\rho^2}[|f_1^0|^2+2\rho^2|f_3^0|^2+2\sqrt{2}\rho|f_1^0|$$
$$\times|f_3^0|\cos(\varphi+\delta\omega t-\varphi_0)]\ , \qquad (4.4)$$

where f_1^0 and f_3^0 are the modal amplitudes at a reference time which, for simplicity, is $t=0$, and φ_0 is the relative phase between f_3^0 and f_1^0. Hence the intensity pattern performs a regular clockwise rotation around the laser axis. When, by contrast, mode $(0,+1)$ is activated, the rotation is counterclockwise, as depicted by the sequence in Fig. 9.

From Fig. 9 one can observe that there is a point in the transverse plane where the electric-field intensity vanishes. This point is the center of an optical vortex [26,17] located at a distance $|f_1^0|/\sqrt{2}|f_3^0|$ from the laser axis. Hence the vortex moves in a circular orbit around the optical axis, with angular frequency $\delta\omega$.

The moduli of amplitudes f_1 and f_3 vary in a continuous way as a function of the control parameters: with reference to Fig. 4(a), for example, we have $f_3=0$ $(f_1=0)$, corresponding to the upper (lower) boundary of region 2. Upon crossing the upper boundary in the downward direction, one encounters a spontaneous breaking of the cylindrical symmetry in the intensity pattern, and simultaneously the breaking of the time-translational symmetry because the pattern in region 2 is rotating [22]. By decreasing the mode spacing η in region 2, $|f_3|$ increases and $|f_1|$ decreases, so that the vortex circles closer and closer to the origin and, when the

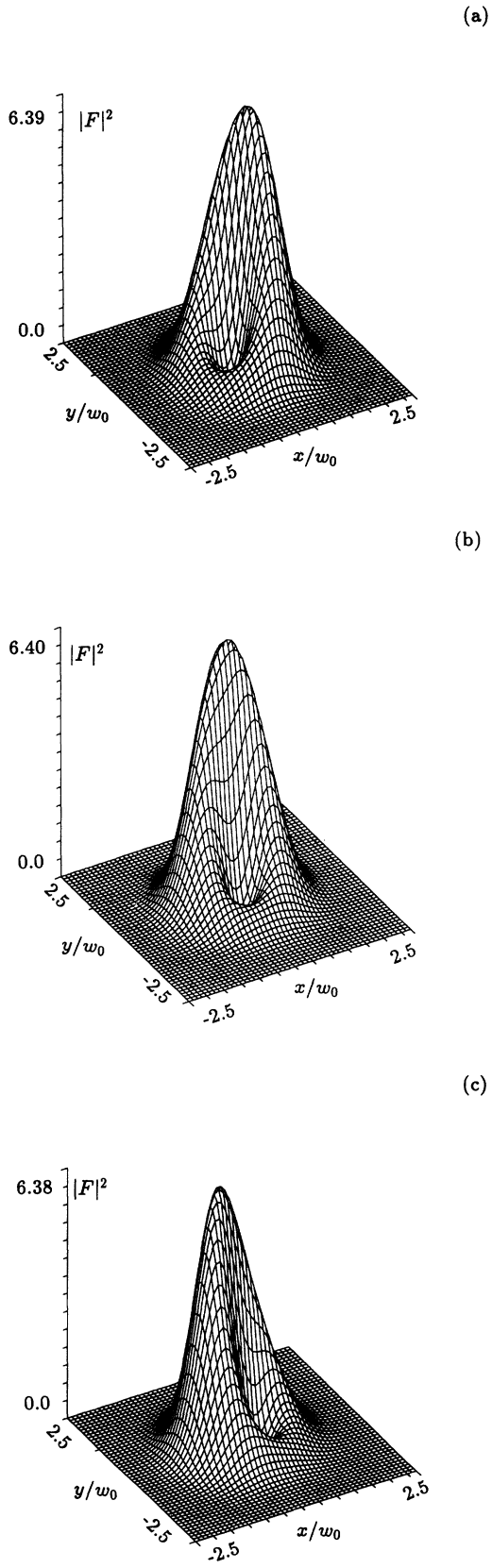

FIG. 9. Three-mode laser (Na_2 parameters, $\psi=1.63$, $2C=9.66$, $\Delta=1.76$, and $\eta=4.3$). Plot of the transverse intensity profile for the traveling-wave pattern [Eq. (4.4)] at three subsequent times. The vortex rotation is evident.

lower boundary is reached, it is located exactly at the origin, and the pattern becomes a pure, stationary, doughnut mode.

The first experimental observation of a transverse rotating pattern in a nonlinear optical system was obtained by Giusfredi *et al.* [6] in a passive Na system with a single mirror configuration; other experimental observations, directly related to our numerical results, will be discussed in paper II.

Configuration (4.4) represents a traveling wave in the angular variable. In the following we will label as "standing wave" the configuration in which both doughnuts $\exp(\pm in\varphi)$ are activated simultaneously with equal (or nearly equal) intensities [it must be kept in mind, however, that due to the frequency beating with modes different from the two doughnuts $\exp(\pm in\varphi)$, these patterns are not stationary but dynamical].

C. Three-mode laser: CO_2 parameters, traveling wave, and alternated rotation

A second set of parameters, fitting the estimated values for the experiment using a CO_2 laser (see paper II), has been explored. Here the relaxation rates are $\tilde{k}=0.3$ and $\tilde{\gamma}=0.01$. In this case the results obtained in Sec. III for the limit $\tilde{\gamma}\ll 1$ provide a good guideline [see Figs. 3(b) and 4(b)]. As in the previous case, upon destabilization of the TEM_{00} mode, one encounters a rotating pattern with the spinning vortex.

A different but related kind of dynamical patterns has been found for $\delta_{AC}=0.9$ and $2C=3.5$: here all the intensities of the three modes have a significant dynamical evolution, and two well-separated time scales are recognizable (Fig. 10). On the short-time scale the behavior is similar to that of the usual rotating pattern, because the intensity of one doughnut mode is negligible; this time scale is given by the inverse of the mode-pulled frequency difference between the doughnut and fundamental modes. On the longer time scale (several hundred times the rotation period) there is a periodic exchange in the role of the two doughnut modes, while the intensity of the fundamental mode undergoes modest variations. Therefore we have an alternation between two rotating patterns, one exhibiting a clockwise spinning vortex, the other a counterclockwise one. This is very simple example of the phenomenon of periodic alternance that was defined by Arecchi *et al.* [20]. The periodic alternating effect has been observed experimentally in a laser with a saturable absorber [39], and in a cavity containing a photorefractive medium [20].

D. Six-mode laser: CO_2 parameters

In this subsection we consider physical conditions in which the laser line activates the six modes where $q=0$, 1, and 2 only. In this case, in addition to the modes described by Eqs. (3.1), (3.2), and (3.3), we have the modes of the family $q=2$, i.e.,

$$A_4=A_{1,0}=\left[\frac{2}{\pi}\right]^{1/2}(1-2\rho^2)e^{-\rho^2}, \tag{4.5}$$

$$A_5=A_{0,2}=\left[\frac{1}{\pi}\right]^{1/2}2\rho^2e^{-\rho^2}e^{+2i\varphi}, \tag{4.6}$$

$$A_6=A_{0,-2}=\left[\frac{1}{\pi}\right]^{1/2}2\rho^2e^{-\rho^2}e^{-2i\varphi}. \tag{4.7}$$

The increased number of dynamical variables leads to a striking richness of dynamical patterns; the most interesting of those will be reviewed briefly in the following.

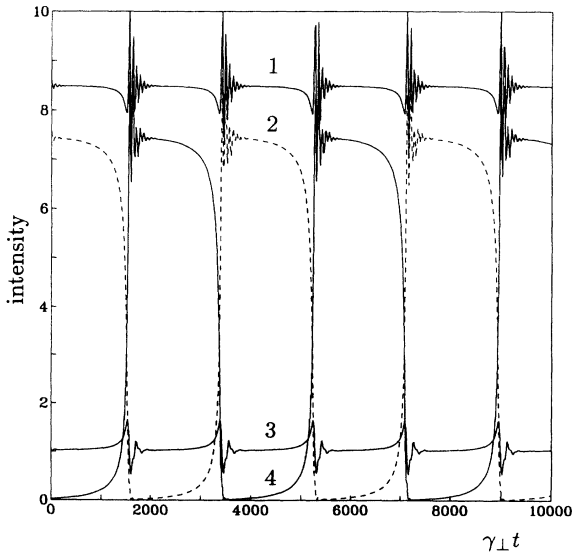

FIG. 10. Three-mode laser (CO_2 parameters $\psi\to\infty$, $2C=3.5$, $\Delta=0.69$, and $\eta=1.95$). Periodic alternance. Line 1 describes the total intensity, lines 2 and 4 describe $|f_3|^2$ and $|f_2|^2$, respectively, and line 3 describes $|f_1|^2$.

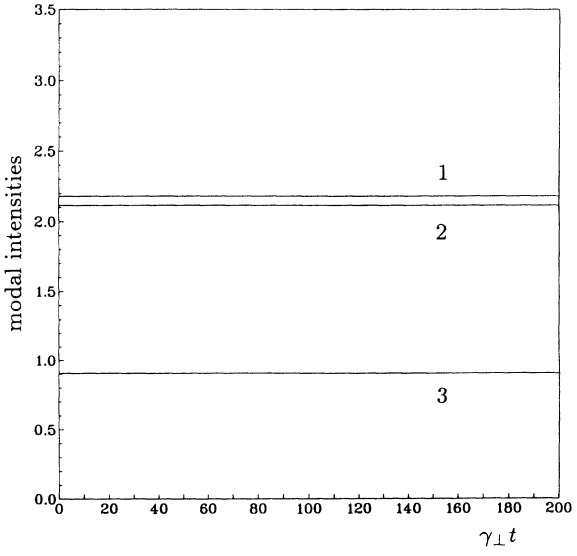

FIG. 11. Six-mode laser (CO_2 parameters, $\psi=2.5$, $2C=3$, $\Delta=-0.154$, and $\eta=0.09$). Double traveling wave. Time evolution of the modal interstitial for modes $(0,+2)$ (line 1), TEM_{00} (line 2), and $(0,+1)$ (line 3).

1. *Double traveling wave*

In this case there are three active modes: the TEM_{00}, the $(0,+1)$, and the $(0,+2)$ modes [or the $(0,-1)$ and $(0,-2)$ modes]; Fig. 11 shows the relative intensities of the modal amplitudes, which do not exhibit oscillations. This pattern presents two rotating vortices located on circular paths centered on the optical axis. The rotation frequency of the vortices is about the mode-pulled frequency spacing between families $q=1$ and 2. Figure 12 shows the intensity evolution at two diametrically opposed fixed points in the transverse plane. The intensities plotted clearly show two frequencies: one is the mode-pulled frequency we mentioned above, the other is twice the first. Finally, Figs. 13(a) and 13(b) display the transverse intensity profile for this pattern, as viewed from two opposite sides, evidencing both vortices.

2. *Traveling wave plus standing wave I: Vortex precession*

This pattern is characterized by a dominant (1,0) mode and by the presence of both $(0,\pm2)$ modes together with a $(0,-1)$ $[(0,+1)]$ mode of about the same magnitude, while the other doughnut mode $(0,+1)$ $[(0,-1)]$ and the TEM_{00} are negligible. As shown in Fig. 14, the modal intensities display small oscillations, and the two $(0,\pm2)$ modes have almost equal intensities. This situation corresponds to the presence of a traveling wave involving the family $2p+|l|=1$ and a standing wave of the family $2p+|l|=2$. The phase of modes belonging to families $q=0$ and 2 rotate with the same frequency, while the phases of modes belonging to the family $q=1$ exhibit a rotation frequency, relative to the former, equal to the mode-pulled frequency spacing between adjacent families.

Because of the orthonormality of the modes [Eq. (2.7)], the total intensity of the field is equal to the sum of the intensities of each mode, and therefore it is not affected by phenomena of interference between modes. The power spectrum of the intensity (Fig. 15) at a point of maximum average intensity (point A in Fig. 17) shows the presence of two main frequencies: $\omega_1=2.34\times10^{-2}\gamma_\perp$ and $\omega_2=0.177\gamma_\perp$. We note that ω_2 is close to the mode-pulled frequency spacing between families 0 and 1, and to the oscillation frequency of the modal intensities. There is no evident interpretation for ω_1.

Within this pattern there are always four vortices moving in the transverse plane. Their motion evolves over two well distinguishable time scales due to the presence of frequencies ω_1 and ω_2. On the short-time scale (linked to the frequency ω_2), the vortices describe small loops symmetrically arranged around the origin; these loops are not closed orbits, however, because on the longer time scale (linked to the frequency ω_1) they undergo a precession around the origin. The two motions can be appreciated in Figs. 16(a) and 16(b), respectively.

Figure 17 is an average of the time-dependent intensity distribution on a time interval equal to the long-time

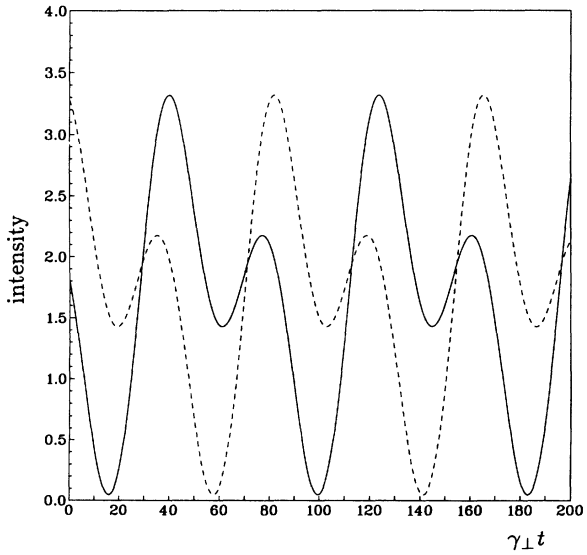

FIG. 12. Six-mode laser, double traveling wave. Time behavior of the intensity at two diametrically opposed points in the transverse plane.

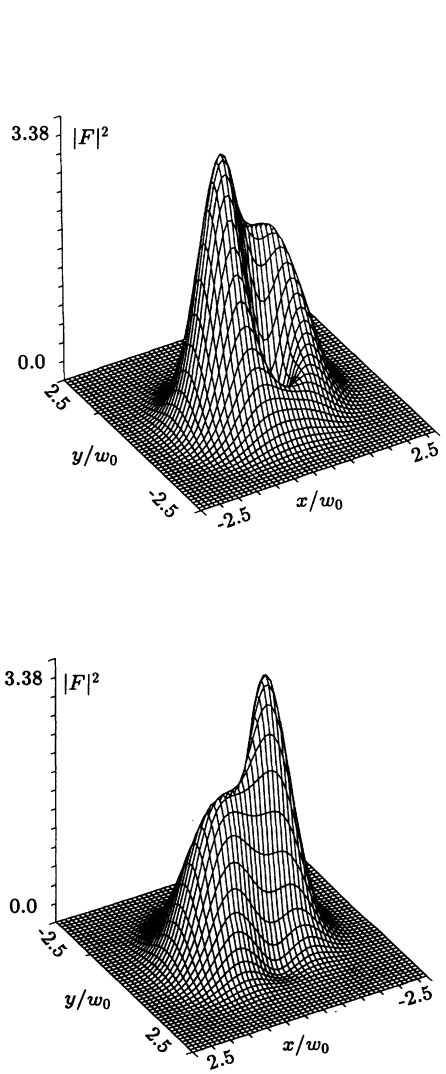

FIG. 13. Six-mode laser, double traveling wave. Transverse intensity profile seen from two opposite viewpoints.

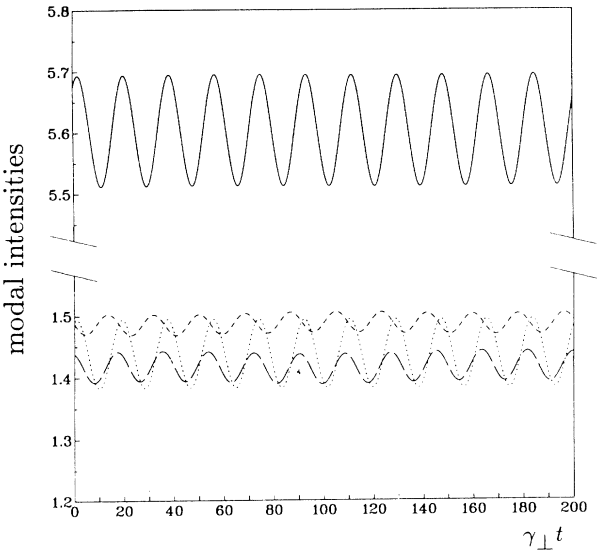

FIG. 14. Six-mode laser (CO_2 parameters, $\psi \to \infty$, $2C=2.5$, $\Delta=0.23$, and $\eta=0.21$). Traveling plus standing wave I. Time evolution of the modal intensities for modes (1,0) (solid line), $(0,-1)$ (dotted line), $(0,+2)$ (short-dashed line), and $(0,-2)$ (long-dashed line).

scale, and shows a central bright spot surrounded by a ring on which four less bright spots are superimposed; this structure has been observed on a fluorescent screen which reveals the structure of the beam emitted by a CO_2 laser, as described in paper II. The last two figures [Figs. 18(a) and 18(b)] show the intensity evolution at two fixed points in the transverse plane. Figure 18(a) refers to intensities recorded at points *A* and *C* of Fig. 17: it is clear that the intensities are in counterphase on the short-time scale, while they are in phase on the long-time scale; Fig. 18(b) shows the same when the intensities are recorded at

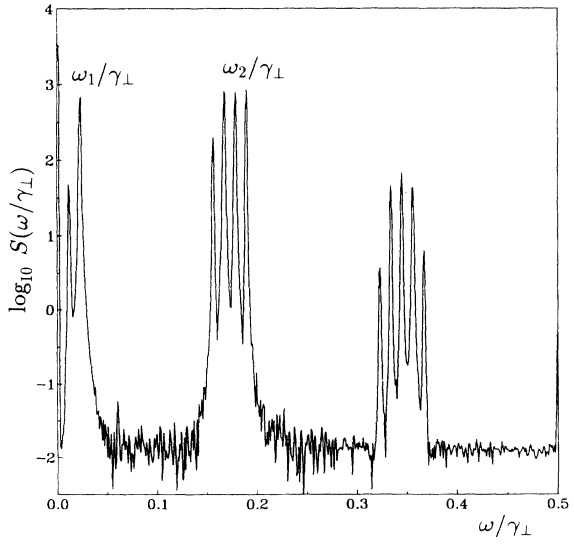

FIG. 15. Six-mode laser, traveling plus standing wave I. Power spectrum of the intensity at point *A* of Fig. 17.

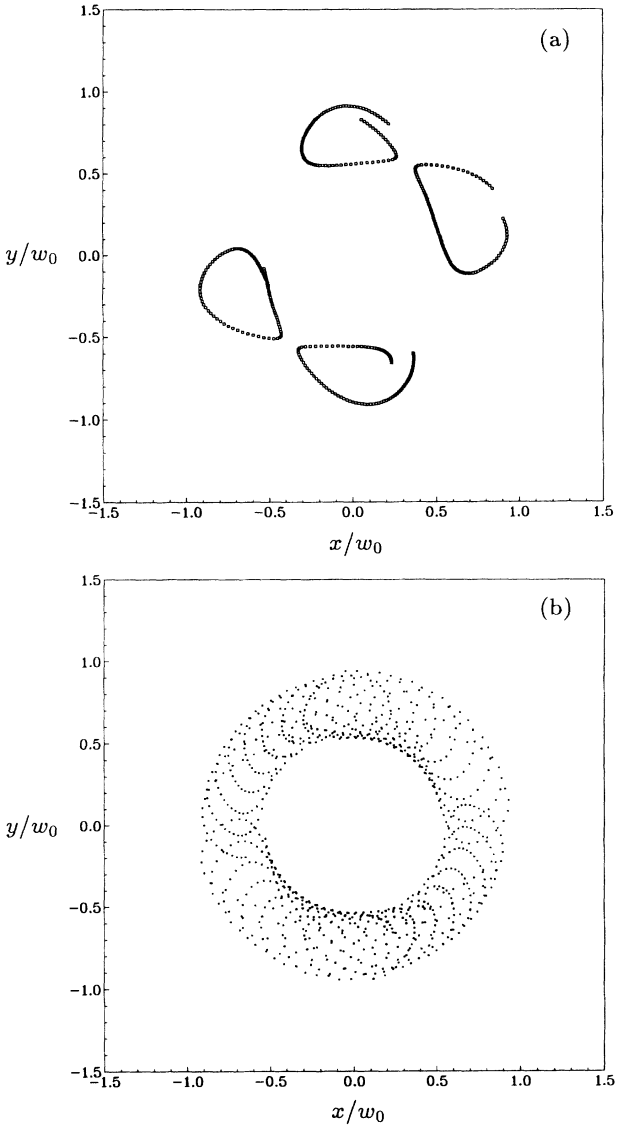

FIG. 16. Six-mode laser, traveling plus standing wave I. Motion of the four vortices (a) on a short time scale, and (b) on a long time scale.

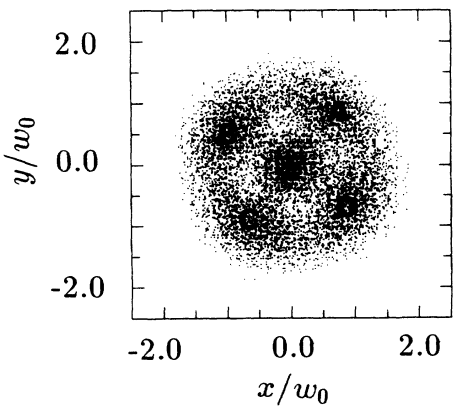

FIG. 17. Six-mode laser, traveling plus standing wave I. Average intensity distribution in the transverse plane; points *A*, *B*, *C*, and *D* mark the secondary maxima of the pattern.

points B and D of Fig. 17. The experimental results presented in paper II are in excellent qualitative agreement with this picture.

3. *Traveling wave plus standing wave II: Creation and annihilation of vortices*

The modal structure of this pattern is similar to the previous case, but here the intensity of the $(0,-1)$ $[(0,+1)]$ mode is much larger than that of the two $(0,\pm 2)$ modes (Fig. 19). Again the larger fundamental frequency ω_2 in the power spectrum of the intensity (Fig. 20) in a point of maximum average intensity corresponds to the mode spacing between families 0 and 1, and there is a smaller fundamental frequency $\omega_1 = 3.66 \times 10^{-3}$ not clearly linked to the characteristic frequencies of the system. The averaged intensity distribution is similar to that of Fig. 17, and the oscillations of the intensity in the opposite secondary maxima are also similar to those shown in Figs. 18(a) and 18(b).

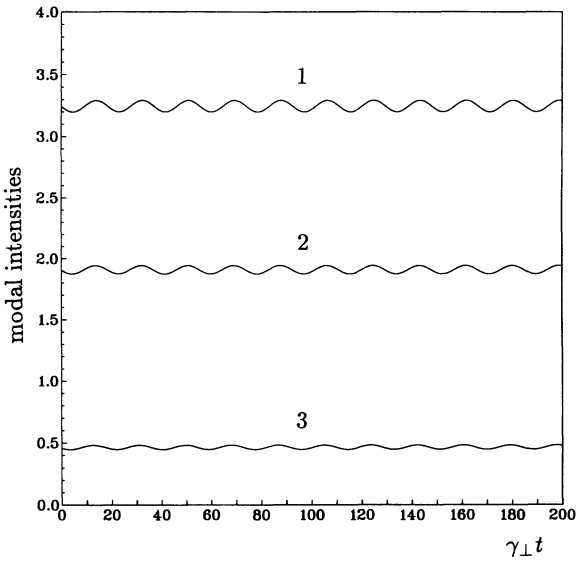

FIG. 19. Six-mode laser (CO_2 parameters, $\psi \to \infty$, $2C = 2.0$, $\Delta = 0.115$, and $\eta = 0.21$). Traveling plus standing wave II. Time evolution of the modal intensities for modes (1,0) (line 1), $(0,+1)$ (line 2), and $(0,\pm 2)$ (line 3).

The peculiarity of this pattern is the motion of the vortices, as Fig. 21 shows: one of them covers a small loop around the origin, while on a larger loop outside it, there are two points (A and C) where a pair of vortices is created, and two others (B and D) where a pair is annihilated. The vortex in the inner orbit has topological charge [17,26] $+1$, while a pair of vortices of opposite charge is created or annihilated on the outer orbit; on the

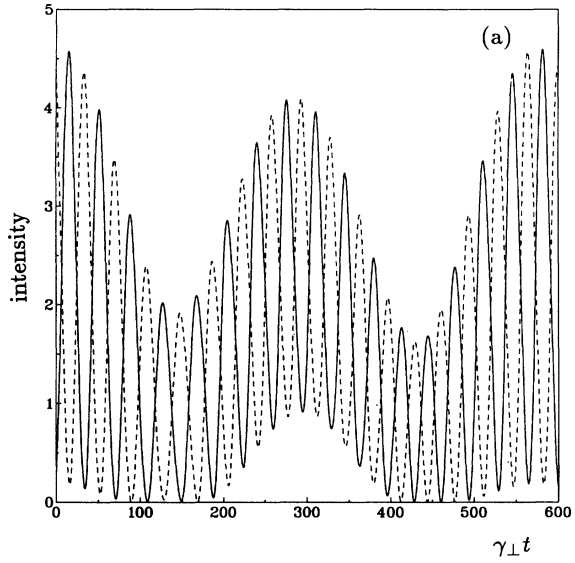

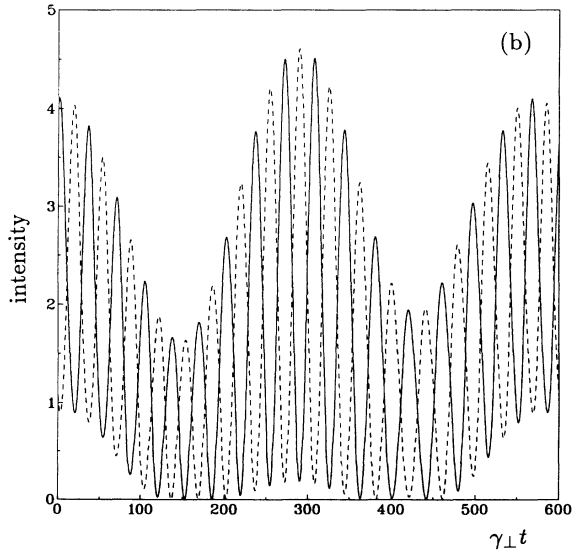

FIG. 18. Six-mode laser, traveling plus standing wave I. Time dependence of the intensity (a) at points A and C, and (b) at points B and D (see Fig. 17).

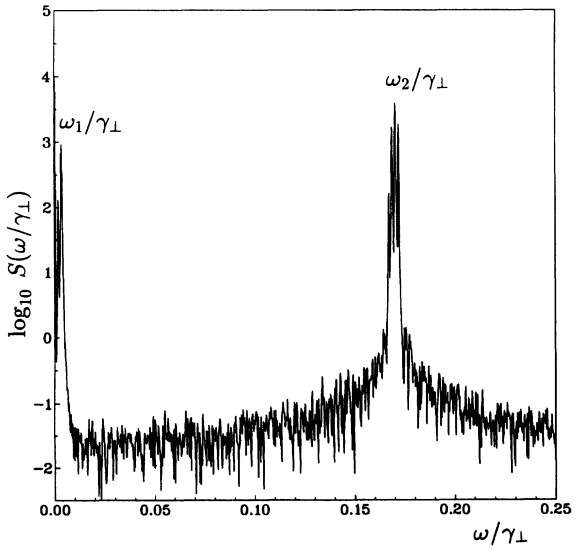

FIG. 20. Six-mode laser, traveling plus standing wave II. Power spectrum of the intensity in a point of maximum average intensity.

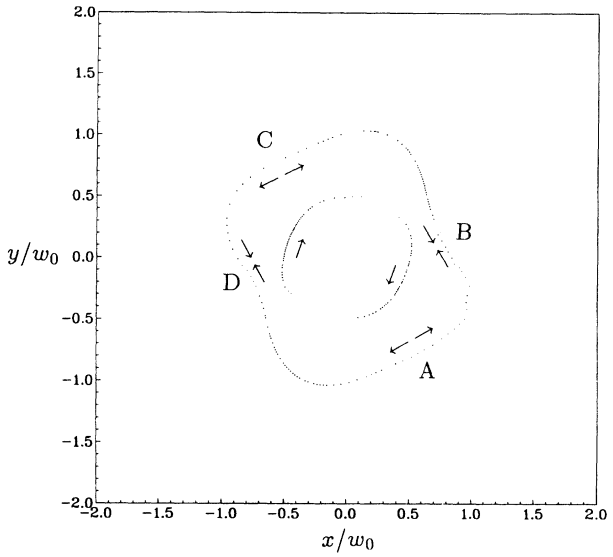

FIG. 21. Six-mode laser, traveling plus standing wave II. Pairs of vortices are periodically created in points A and C, and annihilated in points B and D.

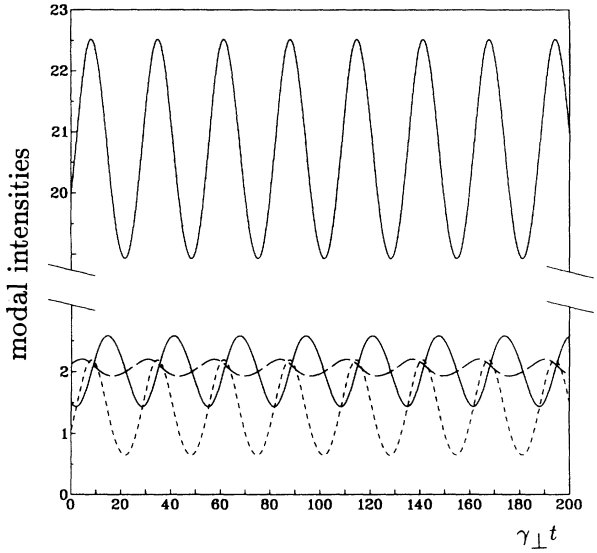

FIG. 22. Six-mode laser (CO_2 parameters, $\psi \to \infty$, $2C=5.0$, $\Delta=-0.154$, and $\eta=0.09$). Standing plus standing wave. Time evolution of the modal intensities for modes (1,0) (upper solid line), TEM_{00} (lower solid line), $(0,\pm1)$ (short-dashed line), and $(0,\pm2)$ (long-dashed line).

latter the total topological charge is always -1, so that the total charge of the pattern is always zero. The motion of the vortices undergoes significant accelerations (decelerations) when the two vortices of a pair are close to an annihilation (creation) point, due to the existence of attractive forces between optical vortices with charges of opposite sign, similar to the forces described in Ref. [40] for the case of the Ginburg-Landau equation.

4. *Standing wave plus standing wave*

In this pattern all six modes are significantly present; the (1,0) mode dominates, and the two elements in each couple of doughnut modes have the same intensity (Fig. 22) and therefore form two standing waves. Moreover, all modes exhibit oscillations where only one fundamental frequency $\bar{\omega}$ (about 15% smaller than twice the mode-pulled spacing between families 0 and 2) is present, as one can see in the power spectrum of the total intensity (Fig. 23).

As in the case of Sec. IV D 2, only the phases of family $q=1$ exhibit a rotation with respect to those of families $q=0$ and 2; the frequency of this rotation is close to the mode-pulled spacing between families $q=0$ and 2. Figure 24 shows the average intensity distribution and the two pairs of opposite points where intensity oscillations have been calculated. The existence of only the fundamental time scale is reflected by the absence of envelope modulation of the intensity oscillations [Figs. 25(a) and 25(b)]. The oscillations in A and C [Fig. 25(a)] are basically in phase and display two frequencies $\bar{\omega}/2$ and $\bar{\omega}$, while in points B and D [Fig. 25(b)], where the oscillations are in counterphase, only $\bar{\omega}/2$ is present.

Again, we have observed creation and annihilation of pairs of vortices, which now move on separated and symmetrical orbits (Fig. 26). To describe their motion, let us suppose we start at a time where two vortices, say v and v', are passing through points a and a', respectively. On the other orbit, at the same instant, a pair of oppositely charged vortices are annihilated at point b. For some time the two vortices v and v' are the only ones surviving until they reach points c and c', respectively; at that moment, a pair w and w' is created at point d. The motion continues until v and v' annihilate at point e and, correspondingly, w and w' are located at points f and f', symmetrical with respect to a and a' on the other orbit. Then the evolution repeats itself symmetrically, on a time scale equal to the period of the oscillations in points B and D of Fig. 24, i.e., $4\pi/\bar{\omega}$.

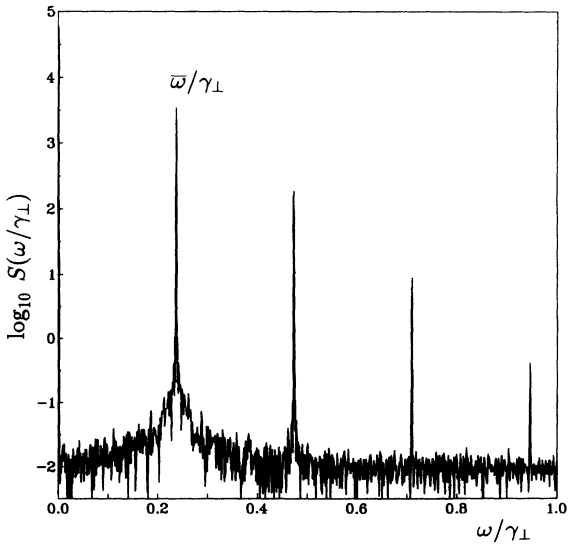

FIG. 23. Six-mode laser, standing plus standing wave. Power spectrum of the total intensity.

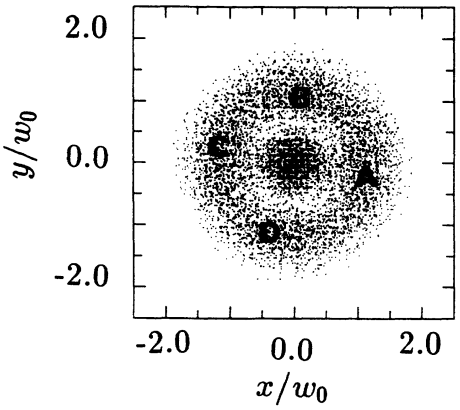

FIG. 24. Six-mode laser, standing plus standing wave. Average intensity distribution in the transverse plane; points A, B, C, and D mark the secondary maxima of the pattern.

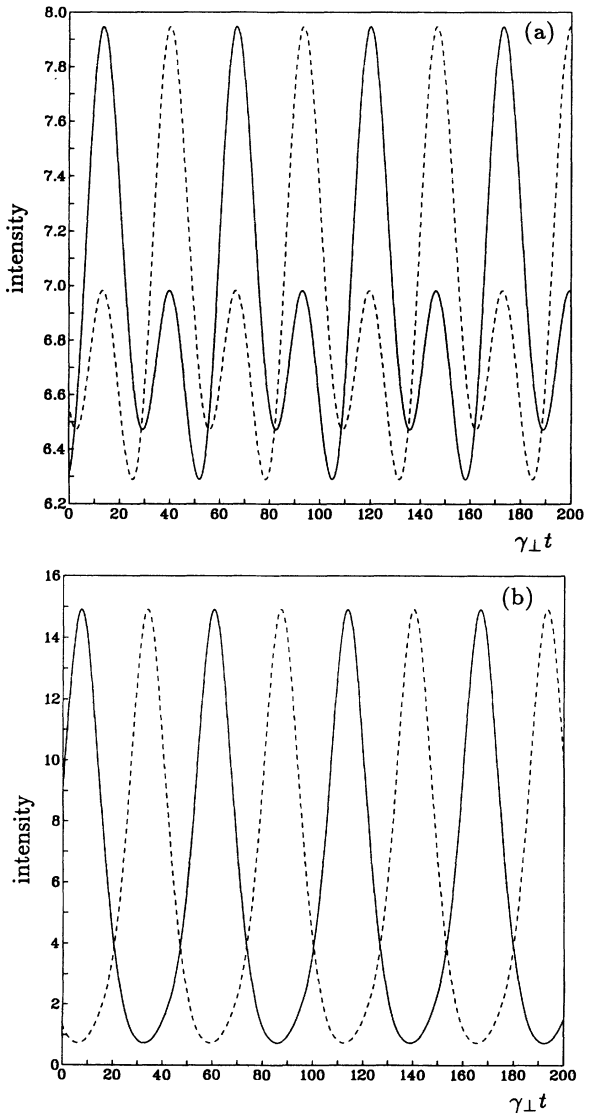

FIG. 25. Six-mode laser, standing plus standing wave. Time dependence of the intensity (a) at points A and C, and (b) at points B and D (see Fig. 24).

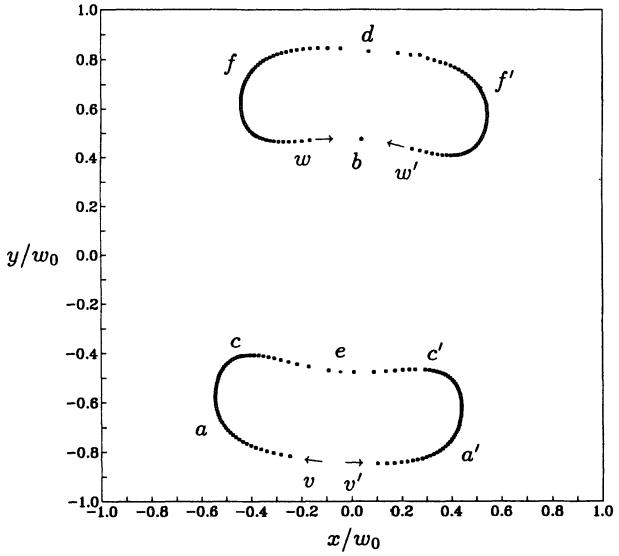

FIG. 26. Six-mode laser, standing plus standing wave. Vortices w and w' are created in point d and annihilated in point b.

E. Removal of frequency degeneracy for a family of modes

Patterns described throughout Secs. IV B, IV C, and IV D offer direct confirmation of some predictions made by group-theory analysis about possible symmetry breaking of cylindrically symmetric systems [22]. Nevertheless, so far it has been impossible to detect in our simulations two other patterns predicted by this approach as steady solutions, namely the simple standing wave [in which, in addition to the fundamental mode, also the two doughnut modes $(0,\pm1)$ are activated with equal intensity] or the standing wave $(0,\pm1)$ plus traveling wave $(0,+2)$ [or $(0,-2)$]. This fact is related to an intrinsic instability of these solutions due to the symmetries of our equations. For certain ranges of parameters and initial conditions, for example, cylindrically symmetric initial conditions evolve to asymmetric standing-wave patterns of the kind requested. These solutions, however, lose their stability by generic perturbations as small as 1% of the total intensity. This behavior has also been confirmed by simulations of the complete set of Maxwell-Bloch partial differential equations [41,30b], thus ruling out the limited number of modes in our calculations as the source of a spurious effect. The discrepancy between our theory and experimental observations of standing-wave patterns can, however, be explained by the intrinsic cylindrical symmetry of our equations (not necessarily of their solutions), impossible to achieve in experimental realizations. In fact, we have been able to stabilize standing-wave solutions by breaking this symmetry via the introduction of a frequency shift for modes of the family $2p+|l|=1$.

In order to describe these patterns in terms of modes, it is useful to switch from the complete set of modes (3.1)–(3.3) to its equivalent form defined as follows:

$$\tilde{A}_1 = A_{0,0} = \left[\frac{2}{\pi}\right]^{1/2} e^{-\rho^2}, \tag{4.8}$$

$$\tilde{A}_2=(A_{0,1}+A_{0,-1})/\sqrt{2}=2\left[\frac{2}{\pi}\right]^{1/2}\rho e^{-\rho^2}\cos\varphi\ , \quad (4.9)$$

$$\tilde{A}_3=(A_{0,1}-A_{0,-1})/\sqrt{-2}=2\left[\frac{2}{\pi}\right]^{1/2}\rho e^{-\rho^2}\sin\varphi\ . \quad (4.10)$$

In our simulations we have assumed that modes 2 and 3 are shifted from the common family frequency by amounts $-\Omega$ and Ω, respectively, equal to a few percent of the mode spacing a_{01} between families 0 and 1. This models small asymmetries of the optical components of the experimental setup which create astigmatism and are responsible for slightly different optical paths for the angularly dependent modes. Actually, mechanisms such as astigmatism or aberration, for example, break the cylindrical symmetry of the system. A precise modeling of these elements would require introducing considerable complications into our equations, and therefore we include such elements in a phenomenological way by introducing a breaking of the frequency degeneracy, as is done here, or differentiated losses, as is done in Sec. IV F.

Simulations performed for both Na_2- and CO_2-like parameters lead to similar results. Overall we can say that when $\Omega\approx(0.03-0.04)a_{0,1}$, one observes stable standing-wave configurations. These patterns are characterized by the presence of a pure cosine (or sine, according to which one has been shifted closer to the atomic frequency) mode superposed to a component of the TEM_{00}. The intensity distribution is given by

$$\begin{aligned}|F(\rho,\varphi,t)|^2&=\frac{2}{\pi}e^{-2\rho^2}|\tilde{f}_1^0+2\rho\tilde{f}_2^0(\cos\varphi)e^{-i\delta\omega t}|^2\\&=\frac{2}{\pi}e^{-2\rho^2}[|\tilde{f}_1^0|^2+4\rho^2|\tilde{f}_2^0|^2\cos^2(\varphi)\\&\quad+4\rho|\tilde{f}_1^0||\tilde{f}_2^0|\cos\varphi\cos(\delta\omega t-\varphi_0)]\ ,\end{aligned} \quad (4.11)$$

where $\tilde{f}_1^0$ and $\tilde{f}_2^0$ are the amplitudes of modes $\tilde{A}_1$ and $\tilde{A}_2$ at a reference time which, for simplicity, is $t=0$, and φ_0 is the relative phase between $\tilde{f}_1^0$ and $\tilde{f}_2^0$. The quantity $\delta\omega$ is given by Eq. (4.3). The relative phase rotates with the usual frequency (4.3): the role of the phase rotation is clarified by Figs. 27(a) and 27(b), where two maxima of the intensity grow and decay alternately during the rotation period; the field intensities corresponding to the two peaks exhibit sinusoidal oscillations in counterphase. The time-averaged intensity pattern is shown in Fig. 28, where two bright spots are clearly visible. More precisely, the numerical calculations show that the modal intensities exhibit small oscillations (Fig. 29), so that in Eq. (4.11) $|\tilde{f}_1^0|$ and $|\tilde{f}_2^0|$ must be replaced by two time-dependent functions which display these oscillations. When Ω is reduced to 1% or 2% of a_{01}, the sine (cosine) mode comes into play and the amplitude of the oscillations of the modal intensities increases. The temporal behavior of the intensities of modes $\tilde{A}_i$ $(i=1,2,3)$ is shown in Fig. 30, while Fig. 31 shows the same for the doughnut modes (3.1)–(3.3). The fundamental oscillation

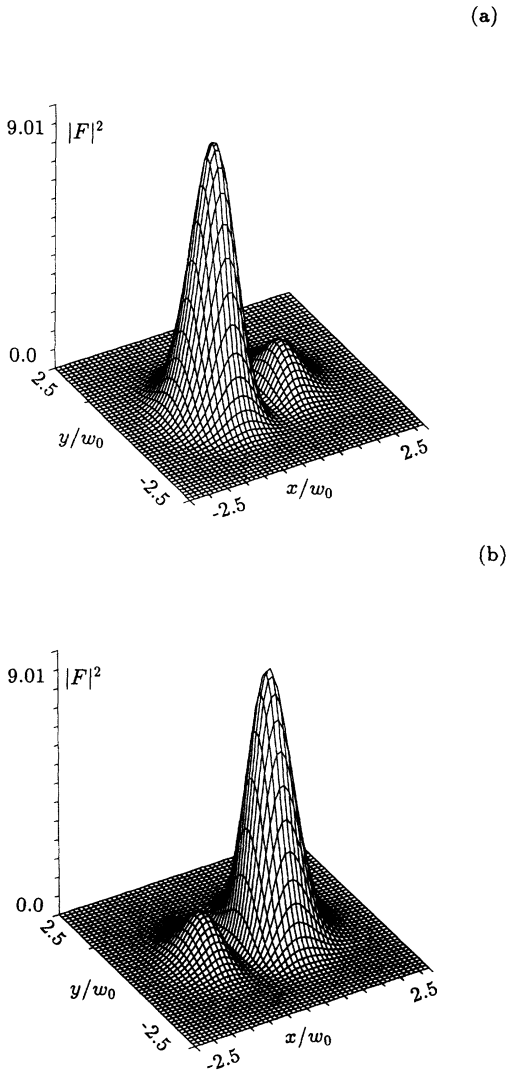

FIG. 27. Three-mode laser with frequency-degeneracy removal. Standing-wave configuration and Na_2 parameters ($\psi=1.63$, $2C=9.66$, $\Delta=2.03$, $\eta=4.3$ and $\Omega=0.04a_{0,1}$). Plot of the transverse intensity profile for the standing-wave pattern [Eq. (4.11)] at two subsequent times.

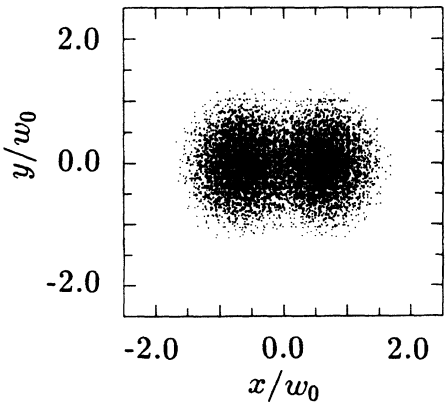

FIG. 28. Three-mode laser with frequency-degeneracy removal, standing-wave configuration. Average intensity distribution in the transverse plane.

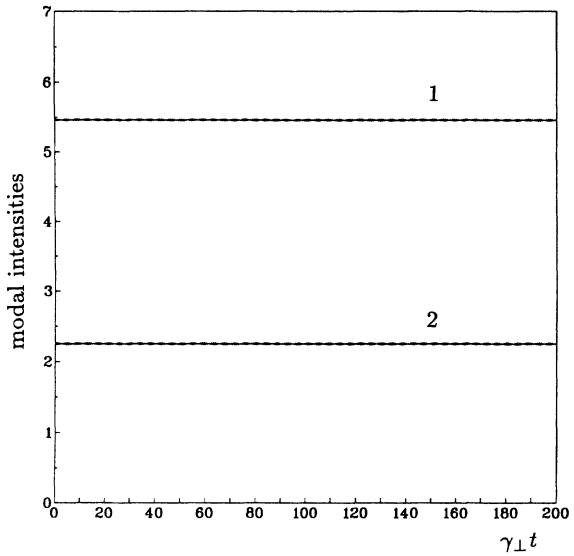

FIG. 29. Three-mode laser with frequency-degeneracy removal. Upper line: intensity of the cosine mode [see Eq. (4.9)]; lower line: intensity of the TEM_{00} mode. Same parameters as in Figs. 27 and 28.

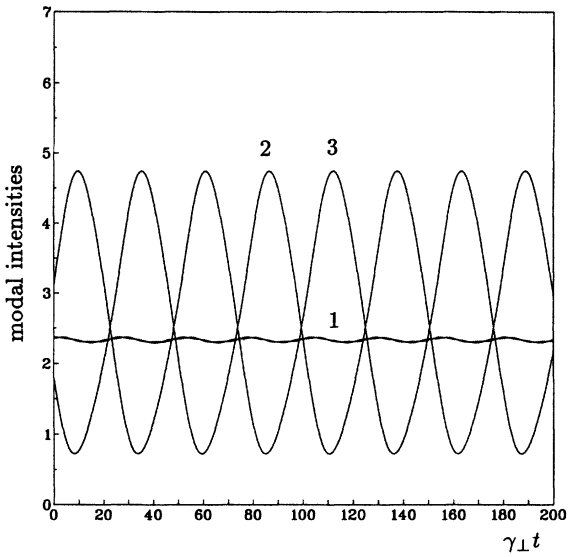

FIG. 31. Three-mode laser with frequency-degeneracy removal. Same dynamical regime as in Fig. 30. The intensities of $(0,+1)$ mode (line 1), TEM_{00} mode (line 2), and $(0,-1)$ mode (line 3) are shown.

frequency of the mode intensities scales well with the mode-pulled separation 2Ω in the Na_2 case, while it appears unrelated to the characteristic time scales in the case of CO_2 lasers. In this regime the features of the traveling and standing waves appear alternately. Specifically, when one of the two doughnuts is dominant the traveling wave prevails, while the standing wave manifests itself when the two doughnuts have the same intensity. This behavior is well described by the motion of the vortex (Fig. 32). It initially moves around the origin describing expanding orbits that eventually go to infinity, and then comes back, circling the other way round (see Fig. 31: the two doughnuts exchange on the long-time scale). Upon further reduction of Ω the sine and cosine modes tend to lock together with about the same intensity, and the pure traveling-wave configuration is restored in the limit $\Omega \rightarrow 0$.

F. Differentiated losses for the modes of the family $q=1$

Another procedure for obtaining the stabilization of the standing-wave pattern is the introduction of two different cavity damping rates for the modes described by

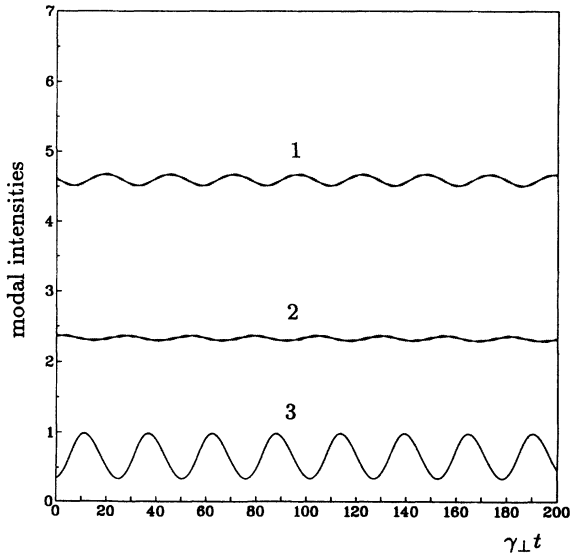

FIG. 30. Three-mode laser with frequency-degeneracy removal. Same parameters as in Fig. 27, but $\Omega=0.02a_{0,1}$. Intensity of the cosine mode, (line 1) TEM_{00} mode (line 2), and sine mode (line 3).

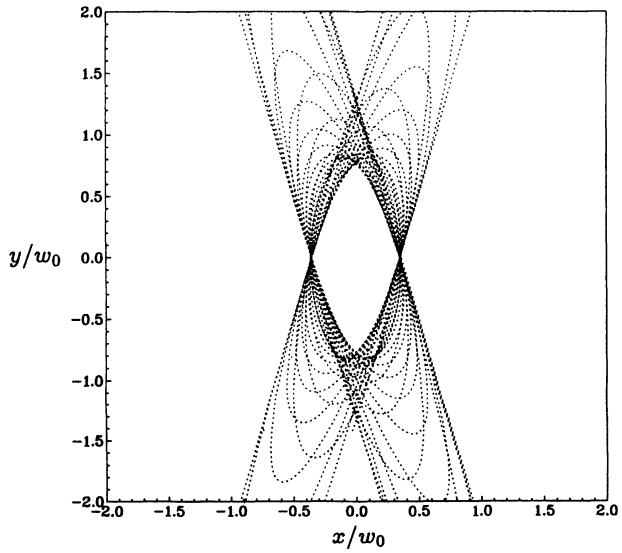

FIG. 32. Three-mode laser with frequency-degeneracy removal. Motion of the vortex in the transverse plane.

Eqs. (4.9) and (4.10). This corresponds to simulating uncompensated astigmatic losses in the laser Brewster windows or in the lenses. The equations for the three modes in play read

$$\frac{d\tilde{f}_1}{dt}=-k\left[f_1-2C\int_0^{2\pi}d\varphi\int_0^{\infty}d\rho\,\rho\,\tilde{A}_1(\rho,\varphi)P(\rho,\varphi,t)\right], \tag{4.12a}$$

$$\frac{d\tilde{f}_2}{dt}=-k\left[(1+ia_{01})f_2 -2C\int_0^{2\pi}d\varphi\int_0^{\infty}d\rho\,\rho\,\tilde{A}_2(\rho,\varphi)P(\rho,\varphi,t)\right], \tag{4.12b}$$

$$\frac{d\tilde{f}_3}{dt}=-k\left[\left(1+\frac{\delta k}{k}+ia_{01}\right)f_3 -2C\int_0^{2\pi}d\varphi\int_0^{\infty}d\rho\,\rho\,\tilde{A}_3(\rho,\varphi)P(\rho,\varphi,t)\right], \tag{4.12c}$$

where $\tilde{f}_i$ $(i=1,2,3)$ is the amplitude of the modal function $\tilde{A}_i$ $(i=1,2,3)$ as given in Sec. IV E. We have numerically integrated these equations, using control parameters values suitable for the Na_2 laser.

Since we assume that mode 2 suffers smaller losses than mode 3, we coherently observe in the temporal evolution that mode 3 rapidly decays to zero, and the final state is made up of a combination of modes 1 and 2. The pattern one observes under these conditions is very similar to that described in Sec. IV E, and its transverse dynamics as well as the average intensity distribution are the same as in Figs. 27 and 28, respectively.

G. Unlocked doughnut

Another dynamical pattern which exhibits a regular alternance among different transverse configurations has been found using the same model as in Sec. IV E, and moving the atomic line closer to family $q=1$, so that the TEM_{00} mode is suppressed. The frequency shift 2Ω between modes 2 and 3 amounts to a few percent of the mode spacing a_{01}, it prevents these modes from locking together and from realizing a stable stationary doughnut pattern [15]. Actually, the two modes exhibit a beat frequency δ (in general close to the frequency shift), and their intensities oscillate with frequency 2δ. In general the behavior of the field intensity is well described by an expression of the form

$$|F|^2\propto\rho^2e^{-2\rho^2}\left|a\sqrt{1+\epsilon_1\sin(2\delta t)}\cos\varphi+b\sqrt{1+\epsilon_2\sin(2\delta t)}(\sin\varphi)e^{i\delta t}\right|^2$$
$$=\rho^2e^{-2\rho^2}\{a^2[1+\epsilon_1\sin(2\delta t)]\cos^2\varphi+b^2[1+\epsilon_2\sin(2\delta t)]\sin^2\varphi+ab\sin(2\varphi)\sqrt{1+\epsilon_1\sin(2\delta t)}\sqrt{1+\epsilon_2\sin(2\delta t)}\cos\delta t\} \tag{4.13}$$

where a^2 and b^2 are the mean values of $|\tilde{f}_2|^2$ and $|\tilde{f}_3|^2$, respectively, and ϵ_1 and ϵ_2 are constants. We note that $a>b$ when the atomic line is closer to mode 2. If one defines $T=2\pi/\delta$, Eq. (4.13) reads

$$|F|^2=\begin{cases}C_1\rho^2e^{-2\rho^2}\cos^2(\varphi-\varphi_0), & t=0\\ C_2\rho^2e^{-2\rho^2}[a^2\cos^2\varphi+b^2\sin^2\varphi], & t=T/4\\ C_1\rho^2e^{-2\rho^2}\cos^2(\varphi+\varphi_0), & t=T/2\\ C_2\rho^2e^{-2\rho^2}[a^2\cos^2\varphi+b^2\sin^2\varphi], & t=3T/4\end{cases}, \tag{4.14}$$

where $\varphi_0=\tan^{-1}(b/a)$, and C_1 and C_2 are constants. From Eq. (4.14) it is clear that the first and third expressions describe two-peaked structures rotated by $2\varphi_0$ with respect to each other, while the second (and fourth) is a pattern whose transverse intensity distribution depends on the ratio b/a.

When the atomic line is centered halfway between modes 2 and 3, one finds $a=b$, so that (a) $\varphi_0=\pi/4$, and the two-peaked structures lie on the two straight lines $y=-x$ and x in the transverse plane, respectively; and (b) the second and fourth structures become independent of φ and correspond to the pure doughnut patterns. In addition, $\epsilon_1=\epsilon_2$, so that the time evolution of the two oscillating modal intensities are perfectly superimposed.

The simulation shown in Fig. 33 uses the parameters for a Na_2 laser, so that a comparison can be made with the experimental data reported in paper II. We plot the local intensity recorded at fixed points in the transverse plane shown in Fig. 34; we begin by noting that the signals at points $P_{1,1}$ and $P_{-1,-1}$ are exactly equal: their maxima correspond to the appearance of the two-peaked structure oriented along $y=x$ $(t=T/2)$, while they drop to zero when the two-peaked structure appears along $y=-x$ $(t=0)$. It turns out that the oscillation frequency is equal to the mode-pulled frequency shift $2\tilde{k}\Omega/(1+\tilde{k})$. The intensity at points $P_{-1,1}$ and $P_{1,-1}$ is in counterphase with respect to the previous couple. The four points on the axes $P_{1,0}$, $P_{0,1}$, $P_{-1,0}$, and $P_{0,-1}$ are not affected by interference between modes 2 and 3, and thus the oscillation amplitudes of the signals are much smaller than in the previous cases, because they arise from the modulation of the amplitudes $|f_2|$ and $|f_3|$, shown in Eq. (4.13). At $t=T/4$ and $3T/4$, the same local intensity is

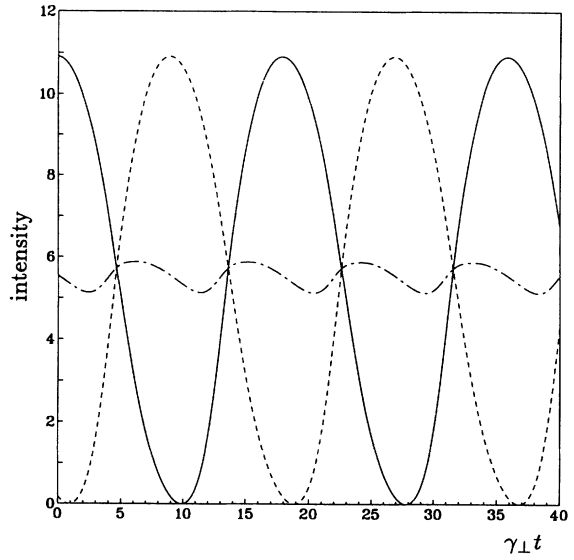

FIG. 33. Unlocked doughnut. Na_2 parameters: $\psi=1.63$, $2C=9.66$, $\Delta=3.5$, $\eta=4.3$, and $\Omega=0.05a_{0,1}$. Local intensity at fixed points in the transverse plane (see Fig. 34). The solid line shows the intensity recorded at points $P_{1,1}$ and $P_{-1,-1}$; the dashed line shows the intensity recorded at points $P_{-1,1}$ and $P_{1,-1}$; and the dotted-dashed line shows the intensity recorded at points $P_{1,0}$, $P_{0,1}$, $P_{-1,0}$, and $P_{0,-1}$.

recorded at all points, corresponding to the appearance of a doughnut pattern which has a symmetrical intensity distribution.

H. Six-mode laser: Nd:YAG parameters

Several plots of the vortex dynamics shown in the previous subsections have already proved the richness and complexity of the laser behavior whenever transverse modes with different frequencies are considered. By focusing on parameter values characteristic of Nd:YAG lasers ($\tilde{k}=0.05$, $\tilde{\gamma}=0.0025$, $\Delta=-0.2$, and $\psi\to\infty$), we now study in more detail a particular, yet generic, transition between dynamical patterns. To illustrate this transition we have kept η fixed at 0.2 while progressively increasing the pump $2C$ [see Fig. 3(c) for the corresponding stability domain of the Gaussian mode].

Close to the instability threshold, the usual single vortex rotating around the beam center is found. Increasing the pump parameter, one observes the intensity of a doughnut mode to grow from zero by removing energy from the Gaussian mode. The vortex then moves toward the center of the beam. One doughnut mode is as likely to grow as the other, because the cylindrical symmetry of the equations does not favor either. In the following we consider the $(0,-1)$ doughnut mode alone as the initial dynamical pattern of the transition under investigation. In this state the off-center vortex initially rotates clockwise. The final state involves only the $(0,-1)$ and (1,0) modes.

At variance with the results of Sec. IV B, a pure

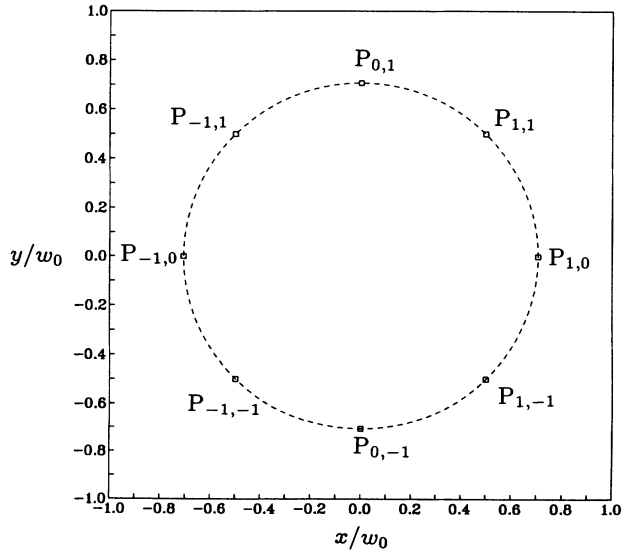

FIG. 34. Location in the transverse plane of the eight points at which the intensities of Fig. 33 have been recorded.

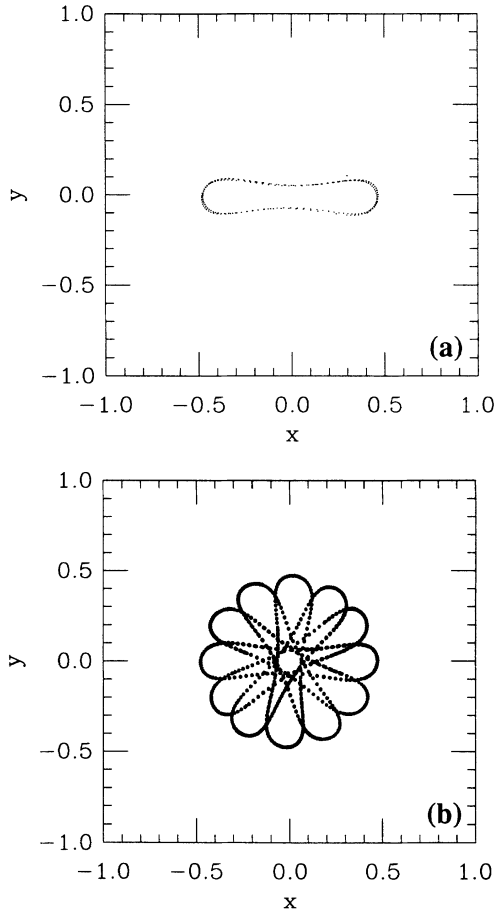

FIG. 35. The "bow-tie-shaped" trajectory of the central vortex observed after the introduction of the (1,0) mode to the dynamics. (a) The short-time scale $[(1+\tilde{k})/\eta]$ orbit of the central vortex. Overlapped on the vortex trajectory is the prediction of Eqs. (4.16). (b) A succession of snapshots of the vortex trajectory, illustrating the precession of the bow-tie on the longer time scale.

$(0,-1)$ stationary state is never recovered. Before the vortex reaches the beam center, the next radially symmetric (1,0) mode grows from zero amplitude (at $2C=1.725...$). The resulting three-mode pattern mediates the transition and is the focus of our analysis. Apart from introducing a new anticlockwise rotating vortex at a large distance from the beam center (see the end of this subsection), the three-mode interaction progressively distorts the initially circular trajectory of the existing vortex so that is acquires a peculiar "bow-tie" shape [see Fig. 35(a)]. The vortex completes this trajectory at almost the same frequency as for the circular path. However, on a longer time scale (about 2000 times slower than the rotation period), the "bow-tie" trajectory precesses in the same sense as the vortex rotates—i.e., clockwise in our case [see Fig. 35(b)]. The intensity distribution for this pattern has the form

$$|F(\rho,\varphi,t)|^2=\frac{2}{\pi}e^{-2\rho^2}|f_1^0+\rho\sqrt{2}f_3^0e^{-i(\varphi+\delta\omega_3 t)} +(1-2\rho^2)f_4^0e^{-i\delta\omega_4 t)}|^2 , \tag{4.15}$$

where f_1^0, f_3^0, and f_4^0 are the amplitudes of modes TEM_{00}, $(0,-1)$, and (1,0), respectively, at time $t=0$, and $\delta\omega_i$'s are the respective frequency differences from the Gaussian mode. From the numerical computations, we observe that the modes oscillate at almost their mode pulled frequencies, i.e., $\delta\omega_3=\frac{1}{2}\delta\omega_4=\delta\omega$, where the latter is given by Eq. (4.3). Under this approximation, Eq. (4.15) reproduces the "bow-tie" vortex trajectory without the precession components, and the motion of the inner vortex is described by the equations

$$X_v=\frac{-\sin(\delta\omega t)\pm\left[\sin^2(\delta\omega t)-\dfrac{4|f_4^0|}{|f_3^0|^2}\cos(2\delta\omega t)[|f_1^0|-|f_4^0|\cos(2\delta\omega t)]\right]^{1/2}}{\dfrac{|f_1^0||f_4^0|\sin(4\delta\omega t)}{|f_3^0|^2\cos(\delta\omega t)}} , \tag{4.16a}$$

$$Y_v=X_v\tan(\delta\omega t)+\frac{|f_1^0|\sin(2\delta\omega t)}{\sqrt{2}|f_3^0|\cos(\delta\omega t)} , \tag{4.16b}$$

where X_v and Y_v are the Cartesian coordinates of the vortex in the transverse plane. A comparison between Eqs. (4.16) and the numerical computation yields an agreement within the line size of Fig. 35(a). However, in order to describe the slow precessing motion, one has to impose $\delta\omega_3\neq\frac{1}{2}\delta\omega_4$. This means that on a short-time scale the modes may be assumed to oscillate at their mode-pulled frequencies, while on a longer time scale smaller frequency shifts become relevant to describe the precession of noncylindrically symmetric vortex trajectories.

The three-mode interaction is still more complicated. Similarly to the vortex precession presented in Sec. IV B, this interaction induces oscillations of the modal intensities. These oscillations are quisiperiodic containing $\delta\omega_3$ and $\delta\omega_4$ and their difference, i.e., the precession frequency.

We have studied the details of the transition from two- to three-mode patterns around $2C=1.725$. Figure 36(a) shows evidence of the Hopf character of the bifurcation as the amplitude of the oscillation grows with the square root of the control parameter $2C$ normalized to the threshold value [42]. The bifurcation is reminiscent of the interaction between purely radial modes as described in Ref. [43]. Similarly, at $2C=2.138$ an inverse Hopf bifurcation occurs corresponding to the vanishing of the Gaussian mode intensity [see Fig. 36(b)]. The final state of the analyzed transition is formed by the $(0,-1)$ and (1,0) modes, where the field intensity distribution has the form

$$\begin{aligned}|F(\rho,\varphi,t)|^2&=\frac{2}{\pi}e^{-2\rho^2}|\rho\sqrt{2}f_3^0e^{-i(\varphi-\delta\omega t)}+(1-2\rho^2)f_4^0|^2\\&=\frac{2}{\pi}e^{-2\rho^2}[2\rho^2|f_3^0|^2+(1-2\rho^2)^2|f_4^0|^2+2\sqrt{2}\rho(1-2\rho^2)|f_3^0||f_4^0|\cos(\varphi-\delta\omega t-\varphi_0)] ,\end{aligned} \tag{4.17}$$

where φ_0 is the fixed relative phase between f_3^0 and f_4^0. The positions of the two vortices can be written simply as follows:

$$\rho_v^{(1)}=\frac{|f_3^0|+\sqrt{|f_3^0|^2+4|f_4^0|^2}}{2\sqrt{2}|f_4^0|}, \quad \varphi_v^{(1)}=\varphi_0+\delta\omega t , \tag{4.18a}$$

$$\rho_v^{(2)}=\frac{-|f_3^0|+\sqrt{|f_3^0|^2+4|f_4^0|^2}}{2\sqrt{2}|f_4^0|} , \quad \varphi_v^{(2)}=\varphi_0+\delta\omega t+\pi . \tag{4.18b}$$

These two vortices are diametrically opposite to each other, and rotate counterclockwise on circular orbits around the beam center with angular frequency $\delta\omega$. The

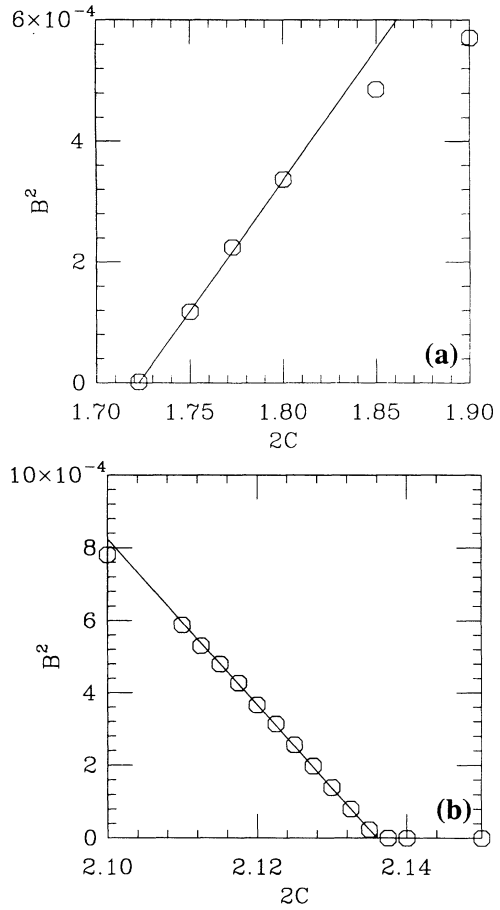

FIG. 36. Demonstration of the Hopf character of the three-mode interaction; the amplitude of oscillation of the total intensity squared grows linearly with the pump. The circular points are measurements taken from numerical simulations and a best-fit straight line was drawn to verify the linear character of the relationship. (a) The Hopf bifurcation associated with the introduction of the (1,0) mode. (b) The inverted Hopf bifurcation associated with the disappearance of the TEM_{00} mode.

three-mode interaction induces a change of the rotation of the vortex close to the beam center. The mechanism at the base of this reversal is inherent in Eqs. (4.15) and (4.17), and is pictured in Fig. 37. The progressive deformation of the "bow-tie" orbit leads to a reversal of the direction of rotation of the vortex without inverting its topological charge. This unexpected behavior proves that for laser patterns which are complex enough (i.e, involving two or more interacting modes), there is no relation between the direction of rotation of the vortices and their topological charge.

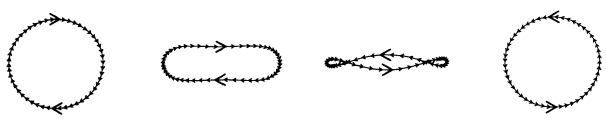

FIG. 37. The trajectory of the inner vortex for successive values of the pump (from left to right $2C=1.75$, 1.79, 1.87, and 2.40). Here the inversion of the sense of rotation intrinsic to this transition is clearly illustrated.

In conclusion, we can summarize the analyzed transition as follows: by a three-mode interaction leading to Hopf oscillations and nontrivial vortex trajectories, the Gaussian mode is replaced by the cylindrically symmetric (1,0) mode in a dynamical pattern involving a doughnut mode.

V. CONCLUDING CONSIDERATIONS

The analysis of this paper aims to continue our previous reports on stationary transverse patterns [10,12–14,17,18]. In Refs. [10,13,14] we considered the case of a frequency spacing among transverse modes of the order of the cavity linewidth, a condition which favors the locking of the modes to a single frequency, which produces a stationary configuration. On the other hand, Refs. [12,17,18] focused on the case of excitation of a single frequency-degenerate family of modes; in this configuration there is no frequency competition and, in the case of class-*A* lasers, the system again approaches a stationary state (this is, however, no longer true for class-*B* lasers, as is shown in Sec. IV A of this paper). The analyses of Refs. [13,14] and Refs. [12,17,18], respectively, were complementary in the sense that in the first group of papers we assumed that the cylindrical symmetry of the pattern is not broken, and therefore we included in our treatment only the modes with $l=0$, whereas in the second group we analyzed specifically the phenomena of spontaneous breaking of the cylindrical symmetry, which arises from the presence of the modes with $l\neq 0$.

In this paper, we include, in principle, modes with whatever values of p and l (without including the restriction $l=0$ of Refs. [13,14] or the restriction $2p+|l|=\text{const}$ of Refs. [12,17,18]), but we focus our analysis on cases in which only a limited number of modes is relevant to the dynamics of the system. The emphasis now is no longer on stationary but on *dynamical* patterns, which become commonplace when the frequency spacing between adjacent transverse modes becomes substantially larger than the cavity linewidth.

Despite the restriction to a dynamics governed by a limited number of modes, the search in the parameter space of the system is quite complex. Our model, which we tried to keep as simple as possible, includes six independent parameters (C, ψ, Δ, η, $k/\gamma_\perp$, and $k/\gamma_\parallel$). For this reason we did not include the possibility of ingredients such as, for example, (i) inhomogeneous broadening, (ii) Fabry-Pérot cavity instead of ring cavity, and (iii) apertures. Concerning point (iii), we observe that in our calculations we have always chosen parametric conditions such that the relevant modes are selected by resonance with the atomic line, so that the inclusion of an aperture is unnecessary (some results obtained using a model which includes an aperture are discussed in Ref. [23]); for the same reason, in most of our calculations we assumed a flat or nearly flat pump profile.

Several of the papers indicated as "early work" in Ref. [9] analyze transverse patterns, observed experimentally, in terms of linear superpositions of a few transverse

modes which beat against one another; the same is also done in Refs. [6,21]. In our approach, instead, we derive the behavior of the system from the nonlinear dynamics of a number of coupled modes, governed by the equations of our model. Even in the very few cases in which the behavior reduces to a superposition of mode amplitudes with constant intensity (see Secs. IV B and IV A), the weights of the superpositions are not assumed *ad hoc*, but derived from the equations. Almost always, in addition, the modal intensities exhibit oscillations as a manifestation of the nonlinear character of the mode-mode interaction; in these cases the dynamics does not reduce to pure mode beating.

Our search was guided by the indications of bifurcation theory [22], which predicts the possible patterns but does not provide informations about their stability. In the case of three-mode dynamics, we performed a fairly complete and mostly analytical linear stability analysis, provided a full characterization of the patterns realized by the laser, and indicated their domains of stability in parameter space. A main point which emerged with evidence is the role of the imperfections in the cylindrical symmetry of the system, which led to the stabilization of patterns that would be unstable in conditions of perfect symmetry. In the case of six-mode dynamics, we identified several (not necessarily all) kinds of patterns. The determination of their domains of existence in parameter space is quite a time-consuming task, which is left for future work.

Our numerical simulations are addressed to three kinds of lasers: Na_2, CO_2, and Nd:YAG (in the last case we analyzed the effects of a negative atomic detuning $\Delta < 0$). Paper II will illustrate some experimental results obtained in Na_2 and CO_2 lasers, and will compare them with theoretical and numerical predictions. However, we observe that the parameter values of simulations for CO_2 lasers do not fit the conditions in the experiment. As a matter of fact, in the experiment the atomic linewidth is very close to the free spectral range, whereas our model assumes that it is smaller. In our simulations, we preferred to consider parameter conditions which ensure strictly the validity of our model, and therefore we considered a laser cavity shorter than that of the experiment by a factor ~ 5. This step has the further benefit that with the shorter cavity the transverse mode spacing can be taken to be of the order of the atomic linewidth, so that relevant modes are selected by resonance with the atomic line, whereas in the experiment they are selected by an aperture. Preliminary investigations for a cavity length closer to that of the experiment show results similar to those illustrated in this paper; however, we do not yet have a complete picture for this case.

The problem of reducing the four-level model for CO_2 lasers to a two-level model was discussed in Ref. [44]. In our numerical simulations we considered a value of $\gamma_{\parallel}$ larger than the real one, in order to make the integration time shorter; in Ref. [44] it is shown that this step does not introduce qualitative differences in the results.

ACKNOWLEDGMENTS

We would like to thank G. D'Alessandro for useful advice. This research was carried out in the framework of the ESPRIT Basic Research Actions TOPP and TONICS. Two of us (A.K. and G.-L.O.) acknowledge partial support from SERC (Gr/F 12665). Two of us (J.R.T. and C.G.) acknowledge partial support from the PACA Region of France and from DRET.

[1] J. H. Moloney, H. Adachihara, D. W. McLaughlin, and A. C. Newell, in *Chaos, Noise and Fractals,* edited by R. Pike and L. Lugiato (Hilger, Bristol, 1988). Early work on this subject was published, e.g., in V. I. Bespolov and V. I. Telanov, Pis'ma Zh. Eksp. Teor. Fiz. **14**, 564 (1971) [JETP Lett. **14**, 390 (1971)]; V. E. Kuzin and A. F. Suchkov, Kvant. Elektron. (Moscow) **2**, 53 (1972) [Sov. J. Quantum Electron. **2**, 236 (1972)].

[2] W. J. Firth, in *Instabilities and Chaos in Quantum Optics,* edited by N. B. Abraham, F. T. Arecchi, and L. A. Lugiato (Plenum, New York, 1988).

[3] W. J. Firth, in *Proceedings of the ECOOSA Conference,* edited by M. Bertolotti and E. R. Pike, IOP Conf. Proc. No. 115 (Institute of Physics, London, 1991), Sec. 3, p. 173.

[4] L. A. Lugiato and R. Lefever, Phys. Rev. Lett. **50**, 220 (1987); M. Brambilla, G. Broggi, and F. Prati, Physica D **58**, 339 (1992).

[5] G. Grynberg, E. Le Bihan, P. Verkerk, P. Simoneau, J. R. R. Leite, D. Bloch, S. Le Boiteux, and M. Duclay, Opt. Commun. **67**, 363 (1988).

[6] G. Giusfredi, J. F. Valley, R. Pon, G. Khitrova, and H. M. Gibbs, J. Opt. Soc. Am. B **5**, 1181 (1988).

[7] S. Akhmanov, M. A. Vorontsov, and V. Y. Ivanov, Pis'ma Zh. Eksp. Teor. Fiz. **47**, 611 (1988) [JETP Lett. **47**, 707 (1988)].

[8] M. LeBerre, E. Ressayre, and A. Tallet, Phys. Rev. A **25**, 1604 (1982), and in Ref. 3, p. 269.

[9] P. Hollinger and C. Jung, J. Opt. Soc. Am. B **2**, 218 (1985); Opt. Commun. **75**, 84 (1990). Early work on this subject was published, e.g., in J. A. Fleck, Jr. and R. E. Kidder, J. Appl. Phys. B **6**, 2327 (1965); I. M. Belousova, G. N. Vinokurov, O. B. Danilov, and N. N. Rozanov, Zh. Eksp. Teor. Fiz. **52**, 1146 (1967) [Sov. Phys. JETP **25**, 761 (1967)]; W. W. Rigrod, Appl. Phys. Lett. **2**, 51 (1963); J. P. Goldsborough, Appl. Opt. **3**, 267 (1964); P. W. Smith, Appl. Phys. Lett. **13**, 235 (1968); D. H. Auston, IEEE J. Quantum Electron **QE-5**, 471 (1968); R. G. Allakhverdyan, A. N. Oraevsky, and A. F. Suchkov, Fiz. Tekh. Poluprovdn. **4**, 341 (1970) [Sov. Phys. Semicond. **4**, 227 (1970)]; L. W. Casperson and E. M. Shekani, Appl. Opt. **14**, 2653 (1975); N. J. Halas, S. N. Liu, and N. B. Abraham, Phys. Rev. A **28**, 2915 (1983); D. J. Biaswas and R. G. Harrison, *ibid.* **32**, 3835 (1985).

[10] L. A. Lugiato, C. Oldano, and L. M. Narducci, J. Opt. Soc. Am. B **5**, 879 (1988).

[11] L. A. Lugiato, F. Prati, L. M. Narducci, P. Ru, J. R. Tredicce, and D. K. Bandy, Phys. Rev. A **37**, 3847 (1988).

[12] L. A. Lugiato, F. Prati, L. M. Narducci, and G.-L. Oppo, Opt. Commun. **69**, 387 (1989).

[13] L. A. Lugiato, G.-L. Oppo, J. R. Tredicce, L. M. Narducci, and M. A. Pernigo, J. Opt. Soc. Am. **7**, 1019 (1990).
[14] J. R. Tredicce, E. J. Quel, A. M. Ghazzawi, C. Green, M. A. Pernigo, L. M. Narducci, and L. A. Lugiato, Phys. Rev. Lett. **62**, 1274 (1989).
[15] C. Tamm, Phys. Rev. A **38**, 5960 (1988).
[16] W. Klische, C. O. Weiss, and B. Wellegehausen, Phys. Rev. A **39**, 919 (1989).
[17] M. Brambilla, F. Battipede, L. A. Lugiato, V. Penna, F. Prati, C. Tamm, and C. O. Weiss, Phys. Rev. A **43**, 5090 (1991).
[18] M. Brambilla, L. A. Lugiato, V. Penna, F. Prati, C. Tamm, and C. O. Weiss, Phys. Rev. A **43**, 5114 (1991).
[19] F. T. Arecchi, R. Meucci, and L. Pezzati, Phys. Rev. A **42**, 5791 (1990).
[20] F. T. Arecchi, G. Giacomelli, P. L. Ramazza, and S. Residori, Phys. Rev. Lett. **65**, 2531 (1990); **67**, 3749 (1991); F. T. Arecchi, in Ref. 3, p. 257.
[21] S. R. Liu and G. Indebetouw, J. Opt. Soc. Am. B **9**, 1507 (1992); G. Indebetouw and S. R. Liu, Opt. Commun. **91**, 321 (1992).
[22] C. Green, G. B. Mindlin, E. J. D'Angleo, H. G. Solari, and J. R. Tredicce, Phys. Rev. Lett. **65**, 3124 (1990).
[23] M. Brambilla, M. Cattaneo, L. A. Lugiato, and F. Prati, in Ref. 3, p. 133.
[24] G.-L. Oppo, L. Gil, G. D'Alessandro, and W. J. Firth, in Ref. [3], p. 191.
[25] L. A. Melnikov, S. Tatarkova, C. N. Tatarkov, J. Opt. Soc. Am. B **7**, 1286 (1990).
[26] P. Coullet, L. Gil, and F. Rocca, Opt. Commun. **73**, 403 (1989).
[27] G.-L. Oppo, M. A. Pernigo, L. M. Narducci, and L. A. Lugiato, in *Measures of Complexity and Chaos,* edited by N. B. Abraham, A. M. Albano, A. Passamante, and P. Rapp (Plenum, New York, 1989), p. 395; L. M. Narducci, G.-L. Oppo, J. R. Tredicce, L. A. Lugiato, and F. Prati, in *Coherence and Quantum Optics VI,* edited by J. H. Eberly, L. Mandel, and E. Wolf (Plenum, New York, 1989), p. 799.
[28] G.-L. Oppo, G. D'Alessandro, and W. J. Firth, Phys. Rev. A **44**, 4712 (1991).
[29] L. Gil, K. Emilsson, and G.-L. Oppo, Phys. Rev. A **45**, 567 (1992).
[30] (a) G. D'Alessandro and G.-L. Oppo, Opt. Commun. **88**, 130 (1992); (b) E. J. D'Angleo, C. Green, J. R. Tredicce, N. B. Abraham, S. Balle, Z. Chen, and G.-L. Oppo, Physica D **61**, 6 (1992).
[31] (a) M. Berry, in *Physics of Defects,* edited by R. Balian *et al.*, Les Houches Session Vol. XXXV (North-Holland, Amsterdam, 1980); (b) N. B. Baranova, B. Ya. Zel'dovich, A. V. Mamaev, N. F. Pilipetskii, and V. V. Shkukov, Pis'ma Zh. Eksp. Fiz. **33**, 206 (1981) [Sov. Phys. JETP Lett. **33**, 196 (1981)].
[32] M. Brambilla, M. Cattaneo, L. A. Lugiato, R. Pirovano, C. Pitzen, and F. Prati, in *Evolution of Dynamical Structures in Complex Systems,* edited by R. Friedrich and A. Wunderlin (Springer, Berlin, 1992), p. 83.
[33] A. B. Coates, C. O. Weiss, C. Green, E. J. D'Angelo, J. R. Tredicce, M. Brambilla, M. Cattaneo, L. A. Lugiato, R. Pirovano, F. Prati, A. J. Kent, and G.-L. Oppo, following paper, Phys. Rev. A **49**, 1452 (1994).
[34] H. Kogelnik, in *Lasers: A Series of Advances,* edited by A. K. Levine (Marcel Dekker, New York, 1966), Vol. 1, p. 295.
[35] H. Lin and N. B. Abraham, Opt. Commun. **79**, 476 (1990).
[36] W. H. Press, B. P. Flannery, S. A. Teukolsky, and W. T. Wetterling, *Numerical Recipes* (Cambridge University Press, Cambridge, 1986).
[37] P. Coullet (unpublished).
[38] N. B. Abraham, Phys. Rev. A **37**, 470 (1988); K. Otsuka, Phys. Rev. Lett. **67**, 1090 (1991); K. Otsuka, P. Mandel, S. Bielawski, D. Derozier, and P. Glorieux, Phys. Rev. A **46**, 1692 (1992); W. Jingy and P. Mandel, *ibid.* **48**, 671 (1993).
[39] D. Hennequin, D. Dangoisse, and P. Glorieux, Opt. Commun. **79**, 200 (1990); Phys. Rev. A **42**, 6966 (1990).
[40] S. Rica and E. Tirapegui, Phys. Rev. Lett. **64**, 878 (1990).
[41] G. D'Alessandro (private communication).
[42] J. Guckenheimer and P. Holmes, *Nonlinear Oscillations, Dynamical Systems, and Bifurcations of Vector Fields* (Springer, New York, 1983).
[43] L. A. Lugiato, G.-L. Oppo, M. A. Pernigo, J. R. Tredicce, L. M. Narducci, and D. K. Bandy, Opt. Commun. **68**, 63 (1988).
[44] G.-L. Oppo, J. R. Tredicce, and L. M. Narducci, Opt. Commun. **69**, 393 (1989).